SHALES AND ABNORMAL PRESSURES

By

J.E. Smith, G.C. Dysinger, and R.L. Borst

TABLE OF CONTENTS

LIST OF TABLES

LIST OF FIGURES

SHALES AND ABNORMAL PRESSURES

By

J. E. Smith, G. C. Dysinger, and R. L. Borst

INTRODUCTION

The various physical circumstances in which pore fluid pressures above and below normal are produced in sedimentary rocks have been clearly described and illustrated by Gretener (1969). The present paper investigates principally gravitational compaction phenomena in shale-sand sequences, including flow and the evolution of pore fluid pressures. Osmotic pressures are also treated quantitatively. Less detailed discussions are given of high pressures in shales produced by gas generation, and by compressive forces deriving from adjacent intruding rocks. Special attention is given to the largest pores in shales, as determined by mercury porosimetry, because of their overwhelming importance in all flow processes and in the mobility of dissolved salt, (Verwey and Overbeek, 1948, p. 66-73).

An historical perspective of the introduction of concepts into the mathematical theory of compaction is included in Helm's (1980) analysis of subsidence due to fluid withdrawal. The present theoretical development allows computations to be carried out such that the compaction, decompaction, and flow throughout each shale unit in a shale-sand section in a gravitational field is followed continuously from the time of deposition. Except for the requirement that the units are flat-lying, the degree of generality is very great: Both shale and sand units are individualized in that the rates of deposition, thicknesses, and rates of erosion are arbitrary, as are grain densities. The sequencing of

the deposition of sand and shale units is also arbitrary, and arbitrary periods of no depositional or erosional activity may be interspersed. Several types of boundary conditions may be applied. Sand between two shales may be treated as a lens, so that the water moving into the sand from one shale moves into the other shale at the same rate. Alternatively, the water pressure in sands may be made time-dependent in special ways, such as the requirement of remaining normally-pressured, or of remaining some fraction of the overburden, or of simply varying in an arbitrary way. This usually results in a net water flow from the shales to the sands, or vice versa, with the excess or deficit water being withdrawn or supplied by a distant lateral source. The requirement of no flow into or out of the bottom of the bottom-most shale in a sequence can also be made. Shales are further individualized through the dependence of permeability on porosity, and through the dependence of porosity on matrix pressure, on compaction history, and on age.

In the numerical examples the shale permeability is usually assumed to be 10^{-6} md at 20 percent porosity, and to vary as the eighth power of the porosity. This agrees well with the experimental trend established by Bryant, Hoffman, and Trabant (1975) for sediments containing more than 80 percent clay and having porosities less than 60 percent. It also tends to agree with their combined data for samples containing clays through silts and having porosities less than 40 percent. At higher porosities the experimentally determined permeabilities are higher. The discrepancies at higher porosities have virtually no effect on the computed examples, as high pressures in shallow, high-porosity clays are ephemeral even with the lower permeabilities assumed here. The data fit recommended by Bryant et al was not suitable for the present application as it extrapolates to 1.3×10^{-6} md at zero porosity. Our extrapolation of shale

permeabilities to increasingly smaller values with decreasing porosity is in conflict with Neglia's (1979) explanation of gas migration from deep, well-consolidated shales by microcracks which develop throughout the shale.

Two expressions have been used in computations to express clay or shale compactibility. The more important follows the experimental work of Skempton (1970) in relating porosity to matrix pressure and to the liquid limit of the individual clay or shale. This correlation has been generalized to take into account the inelastic, partial recovery of porosity when overburden is removed. The second expression used gives the apparent relationship of porosity to matrix pressure and to geologic age of the clay or shale. The geologic age in the expression is a convenient and available stand-in for very complicated processes which go on such as grain deformation and breakage, grain solution and deposition, and mineralogical transformations, e.g., smectite to illite (Burst, 1969). Introduction of geologic age into the relationship between porosity and matrix pressure has the effect of gradualy weakening the grain-to-grain supporting forces. Very high fluid pressures result. These may decrease or increase with time depending on conditions. Both expressions used herein for shale compactibility differ from a previously used expression based on Athy's (1930) work which gave porosity as a function of matrix pressure alone (Smith, 1971; 1973).

GRAVITATIONAL COMPACTION

A. <u>Theory</u>

All lithologies are considered to be deposited as flat-lying units and to remain horizontal during the compaction and fluid flow history. Compactable units do not extrude or compact in the horizontal direction, i.e., there are

horizontal stresses but there are no horizontal strains. Fluid flow in shales is either upward or downward, depending upon the overall pressure regime and may change in magnitude and direction with time. Flow in sands may include upward, downward, and horizontal components as the situation dictates.

Individual shale units are imagined to be divided into sub-units by horizontal planes called nodes (Figure 1). The nodes are time surfaces fixed in the solid matrix; they necessarily move vertically during compaction or dilatation. The distance between successive nodes within a unit varies with time, but the volume of enclosed solid matrix material, R_k, per unit area between any two successive nodes k and k+1 is constant for all times following deposition of the sediments but before their possible erosion:

$$R_k = \int_{Z=U_k}^{Z=U_{k+1}} (1-\phi)dZ = \text{constant in time.} \tag{1}$$

Z is the vertical distance from the base of the sedimentary section (Figure 1). Equation (1) ignores the negligible compressibility of matrix grains. U_k and U_{k+1} are the Z-coordinates of nodes k and k+1, respectively. Throughout these theoretical discussions, ϕ is the fractional porosity rather than the percent porosity.

v_w and v_g are the velocities of water and solid matrix (grains), respectively, relative to the coordinate origin, Z=0. Both are positive for upward movement and negative for downward movement. The mass rates of flow of fluids through nodes k and k+1, per unit area, are given by

$$[(v_w - v_g)\phi\rho_w]_Z = U_k \tag{2}$$

and

$$[(v_w - v_g)\phi\rho_w]_Z = U_{k+1} \quad . \tag{3}$$

ρ_w is the density of water. The mass of fluid between nodes k and k+1, per unit cross-section, is given by

$$\int_{Z=U_k}^{Z=U_{k+1}} \rho_w\phi dZ \quad . \tag{4}$$

The time rate of change of this quantity is equal to the rate of mass flow upward through node k minus the rate of mass flow upward through node k+1;

$$[(v_w - v_g)\phi\rho_w]_k - [(v_w - v_g)\phi\rho_w]_{k+1} = \frac{d}{dt} \int_{Z=U_k}^{Z=U_{k+1}} \phi\rho_w dZ \quad . \tag{5}$$

t is the time.

Darcy's law states that the volume rate of flow of fluid through unit area of sediment, $(v_w - v_g)\phi$, is proportional to the negative gradient of the fluid potential, Ψ, and inversely proportional to the viscosity, η:

$$(v_w - v_g)\phi = -\frac{K}{\eta}\left(\frac{\partial\Psi}{\partial Z}\right)_t \tag{6}$$

The proportionality constant K is called the permeability. The fluid potential gradient, $\partial\Psi/\partial Z$, is the actual fluid pressure gradient $\partial P/\partial Z$, minus the value the gradient would have if the fluid were locally equilibrated, $-g\rho_w$:

$$\left(\frac{\partial\Psi}{\partial Z}\right)_t = \left(\frac{\partial P}{\partial Z}\right)_t + g\rho_w \quad . \tag{7}$$

Thus, Darcy's law becomes

$$(v_w - v_g)\phi = -\frac{K}{\eta}\left\{\left(\frac{\partial P}{\partial Z}\right)_t + g\rho_w\right\} \quad , \tag{8}$$

which allows equation (5) for the rate of change of the mass of fluid between nodes k and k+1 to be written as

$$-\left[\frac{K\rho_w}{\eta}\left\{\left(\frac{\partial P}{\partial Z}\right)_t + g\rho_w\right\}\right]_k + \left[\frac{K\rho_w}{\eta}\left\{\left(\frac{\partial P}{\partial Z}\right)_t + g\rho_w\right\}\right]_{k+1} = \frac{d}{dt}\int_{Z=U_k}^{Z=U_{k+1}}\phi\rho_w dZ \quad . \tag{9}$$

An approximation to equation (9) is obtained by cancelling the linear ρ_w factor:

$$-\left[\frac{K}{\eta}\left\{\left(\frac{\partial P}{\partial Z}\right)_t + g\rho_w\right\}\right]_k + \left[\frac{K}{\eta}\left\{\left(\frac{\partial P}{\partial Z}\right)_t + g\rho_w\right\}\right]_{k+1} = \frac{d}{dt}\int_{Z=U_k}^{Z=U_{k+1}}\phi dZ \quad . \tag{10}$$

The error introduced thereby into the rate of change of the mass of fluid contained between nodes k and k+1 is

$$\left[\frac{(\rho_w)_{Z=U_k}}{(\rho_w)_{Z=U_{k+1}}} - 1\right] \text{ X (rate of flow through node k).} \tag{11}$$

ρ_w will vary from node k to k+1 because of earth temperature and pressure differences. The error is directly proportional to the node spacing and decreases with decreasing spacing. For a large spacing of 100 m(328 feet), a geothermal gradient of 3° C/100 m (1.6^o F/100 ft) and a normal fluid pressure gradient, the quantity in brackets in equation (15) is -0.001. It becomes zero for a fluid pressure gradient about three times normal. The same discrepancy of

-0.001 could result from the weight percent of dissolved salt increasing by 0.14 percent from node k to k+1. The errors introduced by ignoring the variation in ρ_w will usually be of the same order as the uncertainty in the viscosity, η, and will be insignificant compared to uncertainties or errors in the permeability, K, which is extremely sensitive to variations in rock type and porosity as will be shown in the examples. The variables ρ_w, η^{-1} and K have analogous roles in the left hand side of equation (9). By the same type of argument as that following equation (11), little error is introduced by assuming the remaining ρ_w's in the LHS of equation (10) to be constant. Gambolati, Gatto, and Freeze (1974) have included water compressibility in a simpler compaction model and have found it to have little effect.

The right hand side of equation (10) can be simplified with use of equation (1):

$$\frac{d}{dt} \int_{Z=U_k}^{Z=U_{k+1}} \phi \, dZ = \frac{d}{dt} \left[(U_{k+1} - U_k) - \int_{Z=U_k}^{Z=U_{k+1}} (1-\phi) \, dZ \right] \qquad (12)$$

$$= \frac{d}{dt} \left[U_{k+1} - U_k \right]. \qquad (13)$$

Equation (10) may be re-written with this substitution as

$$\left[\frac{K}{\eta} \left\{ \frac{\partial P}{\partial Z} + g\rho_w \right\} - \frac{dU}{dt} \right]_k - \left[\frac{K}{\eta} \left\{ \frac{\partial P}{\partial Z} + g\rho_w \right\} - \frac{dU}{dt} \right]_{k+1} = 0 \; . \qquad (14)$$

The fluid pressure P is the difference between the overburden, S, and the grain-to-grain or matrix pressure, σ:

$$P = S - \sigma \ .$$ (15)

The overburden, S, is the integral of the sediment bulk density, ρ, from the land surface or sea floor to the depth Z, plus the fluid pressure, P_{sw}, at the top of the sedimentary section, $Z = Z_{sw}$:

$$S \equiv g \int_{Z=Z}^{Z=Z_{sw}} \rho dZ + P_{sw} \ .$$ (16)

The bulk density may be written in terms of the porosity, the density of water, and the grain density ρ_g:

$$\rho = \rho_w \phi + \rho_g (1 - \phi)$$ (17)

$$= (\rho_g - \rho_w)(1 - \phi) + \rho_w \ .$$ (18)

With this substitution, equation (16) for the overburden becomes

$$S \equiv g \int_Z^{Z_{sw}} (\rho_g - \rho_w)(1 - \phi)dz + g\rho_w(Z_{sw} - Z) + P_{sw} \ .$$ (19)

With the aid of equations (15) and (19) the quantities in braces in equation (14) may be written in two alternative ways:

$$\left\{ \frac{\partial P}{\partial Z} + g\rho_w \right\} = \frac{\partial}{\partial Z} \left\{ g \int_Z^{Z_{sw}} (\rho_g - \rho_w)(1 - \phi)dZ - \sigma \right\}$$ (20)

$$= - \left\{ g(\rho_g - \rho_w)(1 - \phi) + \frac{\partial \sigma}{\partial Z} \right\} .$$ (21)

The implied differentiation of the integral in equation (20) is carried out exactly in equation (21). The finite difference scheme used in the computations

actually employs equation (20). Substitution into equation (14) gives:

$$\left[\frac{K}{\eta}\frac{\partial}{\partial Z}\left\{g\int_{Z_{SW}}^{Z}(\rho_g-\rho_w)(1-\phi)dZ + \sigma\right\} + \frac{dU}{dt}\right]_k - \left[\frac{K}{\eta}\frac{\partial}{\partial Z}\left\{g\int_{Z_{SW}}^{Z}(\rho_g-\rho_w)(1-\phi)dZ + \sigma\right\} + \frac{dU}{dt}\right]_{k+1} = 0 \ . \quad (22)$$

This result and equation (1) comprise the description of compaction within individual units.

Constitutive equations for the quantities η, σ, and K are needed in computations involving the above expression. In these computations the dependence of η on temperature and salinity is taken from Fabuss and Korosi (1966). Two expressions for σ are used, as discussed in Appendix A. The first (Figure 2) relates σ to porosity and the compaction history through the maximum matrix pressure, σ_{max}, to which the shale has been exposed. It is based on Skempton's (1970) correlations (Figures 3, 4) of plasticity index, PI, with liquid limit, LL, and liquidity index, LI, with matrix pressure. The second (Figure 5) relates σ to the porosity and the age (following deposition) of the shale. Permeability (Figure 6) is computed from

$$K = A\phi^8 \ . \tag{23}$$

B. Boundary Conditions

The vertical pressure gradient through sands within a sedimentary sequence always approximates the hydrostatic or normal gradient, $-g\rho_w$, since the flow rates are small and the adjacent shale units have permeabilities which are smaller by factors of $\sim 10^3$ to $\sim 10^6$. Thus the vertical pressure increase from the top to the bottom of a sand unit of thickness H is

$$+g\rho_w H \ . \tag{24}$$

The thickness H is obtainable from two known factors which are the total zero-porosity thickness, h, and the porosity, ϕ:

$$H = \frac{h}{1-\phi} \quad . \tag{25}$$

The overburden increase from the top to the bottom of the sand is given by

$$g[\rho_w\phi + \rho_g(1 - \phi)]\frac{h}{1-\phi} \quad . \tag{26}$$

The increase in the matrix pressure is the difference between the overburden and fluid pressure increases:

$$g(\rho_g - \rho_w)h \quad . \tag{27}$$

Shale units within the sedimentary sequences are numbered from the bottom as are the nodes. For the remainder of this section, variables may be doubly subscripted to identify them both as to shale unit and node number. The matrix pressure at node k at the top of shale unit ℓ, $\sigma_{\ell,k}$, is greater than the matrix pressure at node k+1 at the bottom of shale unit ℓ+1, $\sigma_{\ell+1,k+1}$, by the quantity (27) summed over any intervening sand units:

$$\sigma_{\ell,k} - \sigma_{\ell+1,k+1} = \sum_{\substack{\text{all} \\ \text{intervening} \\ \text{sands}}} g(\rho_g - \rho_w)h \quad . \tag{28}$$

This result reduces correctly to

$$\sigma_{\ell,k} = \sigma_{\ell+1,k+1} \tag{29}$$

if there are no intervening sands between the shales. It also reduces correctly to

$$\sigma_{\ell,k} = \sum_{\substack{\text{all} \\ \text{overlying} \\ \text{sands}}} g(\rho_g - \rho_w)h \tag{30}$$

if unit ℓ is the uppermost existing shale unit, and as a special case reduces further to

$$\sigma_{\ell,k} = 0 \tag{31}$$

when there are no sands overlying the uppermost shale unit. Thus equation (28) supplies one equation for each shale unit. If, for instance, σ is to be computed from the modified Skempton correlation (Appendix A), this can be signified by writing equation (28) to reflect the independent variables:

$$\sigma(\phi,\sigma_{max},F,LL)_{\ell,k} - \sigma(\phi,\sigma_{max},F,LL)_{\ell+1,k+1} = \sum_{\substack{\text{all} \\ \text{intervening} \\ \text{sands}}} g(\rho_g - \rho_w)h \ . \tag{32}$$

It is seen that (a) this is a relationship between the two unknowns $\phi_{\ell,k}$ and $\phi_{\ell+1,k+1}$ if there is a shale unit $\ell+1$; (b) the mechanical properties of shale units ℓ and $\ell+1$ may be different in that the liquid limits, LL, and decompaction slope parameters, F, may not be the same; and (c) if there is no overlying shale $\ell+1$, equation (32) determines $\phi_{\ell,k}$.

An obvious relationship between the Z-coordinates of nodes k in shale unit ℓ and k+1 in shale unit $\ell+1$ is that they differ by the sum of the constant and known thicknesses of the intervening sands, if any:

$$U_{k+1,\ell+1} - U_{k,\ell} = \sum_{\substack{\text{all} \\ \text{intervening} \\ \text{sands}}} \frac{h}{1-\phi} = \text{constant in time.} \tag{33}$$

This result does not apply if there is no shale unit $\ell+1$. The Z-coordinate at the base of the bottom-most shale unit is always zero:

$$U_{1,1} \equiv 0 \ . \tag{34}$$

A final boundary condition concerns the nature of the fluid flow into or out of the base of each shale unit. Three possibilities are considered for use in computations, although many others are feasible. The first two are special cases of equation (22):

A. If it is required that the bottom-most shale unit in the section overlies an impermeable basement, then equation (22) reduces to

$$\lim_{\substack{Z \to 0 \\ (Z > 0)}} \left[\frac{K}{n} \frac{\partial}{\partial Z} \left\{ g \int_{Z_{sw}}^{Z} (\rho_g - \rho_w)(1-\phi)dZ + \sigma \right\} \right] = 0 . \qquad (35)$$

This condition may be used only for the bottom-most unit.

B. If it is required that the flow into or out of the bottom of shale unit $\ell+1$ is always equal to the flow into or out of the top of shale unit ℓ, i.e., the intervening sands (if any) form a lens, then equation (22) reduces to

$$\lim_{\substack{Z \to U_{k+1,\ell+1} \\ (Z > U_{k+1,\ell+1})}} \left[\frac{K}{n} \frac{\partial}{\partial Z} \left\{ g \int_{Z_{sw}}^{Z} (\rho_g - \rho_w)(1-\phi)dZ + \sigma \right\} \right] -$$

$$\lim_{\substack{Z \to U_{k,\ell} \\ (Z < U_{k,\ell})}} \left[\frac{K}{n} \frac{\partial}{\partial Z} \left\{ g \int_{Z_{sw}}^{Z} (\rho_g - \rho_w)(1-\phi)dZ + \sigma \right\} \right] = 0 . \qquad (36)$$

The time derivatives of the node coordinates $U_{k+1,\ell+1}$ and $U_{k,\ell}$ cancel, by equation (33). This boundary condition can be applied to the base of any of the shale units except the bottom-most unit.

C. A different type of boundary condition and one which may be applied to the base of all shale units is the specification of the fluid pressure as a function of time. In computations, only certain types of fluid pressure time histories have been allowed for. One type of pressure history is computed from the formula

$$P = \alpha(S-P_N) + \beta(P_N-P_{sw}) + P_{sw} \quad, \tag{37}$$

for which one chooses values of the dimensionless constants α and β. During computations variations in the overburden, S, and the normal fluid pressure, P_N, at the base of each unit are monitored. It is not necessary to know the fluid pressure at the sediment surface, P_{sw}, as this does not affect flow and compaction. Equation (37) has been adopted to circumvent the necessity of providing complicated information, such as coefficients to a high order polynomial to specify P as a function of time. This would be a difficult task because the history of sedimentation and erosion of units above the affected shale base might be very erratic. The possibilities of equation (37) are illustrated by noting that for $\alpha=\beta=1$, the pressure is maintained at overburden pressure. For $\alpha=0$ and $\beta=1$ the fluid is maintained at the normal fluid pressure, P_N. The coefficients of α and β are given by

$$(S-P_N) = \sum_{\substack{\text{all}\\ \text{overlying}\\ \text{shales}}} g \int_{\text{bottom of unit}}^{\text{top of unit}} (\rho_g-\rho_w)(1-\phi)dZ + \sum_{\substack{\text{all}\\ \text{overlying}\\ \text{sands}}} g(\rho_g-\rho_w)h \tag{38}$$

and

$$(P_N-P_{sw}) = g\rho_w(U_{sw}-U_{\text{bottom of unit}}) \quad . \tag{39}$$

All quantities on the right hand side of equation (38) are known functions of the time.

It is also possible to specify an arbitrary pressure history for any one specific sand between shale units, following all the deposition and erosion events, and an example is given in Figure 24.

C. Finite Difference Scheme

Table 1 summarizes all the equations governing compaction and boundary conditions for any one shale unit, ℓ, within a sedimentary column. There are two equations for every node in the unit, and the equations for all of the units in the section must be solved simultaneously for the porosity, ϕ_k, and Z-coordinate, U_k, at each node, k. In obtaining the solution to the equations a large matrix must be repeatedly inverted. To make this easier the following change of variables has been introduced:

$$\Delta U_k = U_f - U_k \quad , \quad 1 \leqslant k \leqslant f \quad . \tag{40}$$

The subscript f is the node number at the top of the upper-most existing shale unit. In Table 1 the subscript a is the node number at the bottom of unit ℓ, b is the node number at the top of unit ℓ, a-1 is the node number at the top of shale unit ℓ-1, and b+1 is the node number at the bottom of shale unit ℓ+1. As a mental aid in keeping track of the equations and their significance, each equation is matched with an "associated variable" in the first column of Table 1.

The symbols X_1 through X_{2f-2} represent the quantities on the right hand sides of the equations in Table 1, after the integrals and differentials are replaced by finite-difference approximations. For instance, the first equation becomes

$$X_k = (1 - \frac{\phi_k + \phi_{k+1}}{2}) (\Delta U_k - \Delta U_{k+1}) - R_k \quad , \quad a \leqslant k \leqslant b-1 \quad . \tag{41}$$

Partial derivatives with respect to Z, at a fixed time, are replaced by third order finite difference approximations when there are four or more nodes in a shale unit to allow this. They are replaced by first order finite differences when there are only two nodes in the affected shale unit and by second order finite differences when they are only three nodes.

Total time derivatives of the ΔU_k are always approximated by

$$\frac{d\Delta U_k}{dt} = \frac{\Delta U_k(t) - \Delta U_k(t-\Delta t)}{\Delta t} \quad , \qquad 1 \leqslant k < f \quad , \tag{42}$$

where Δt is the time increment at which successive solutions to the equations are obtained.

Values of ϕ_1 through ϕ_{f-1} and ΔU_1 through ΔU_{f-1} which satisfy the resulting equations $X_1=0$ through $X_{2f-2}=0$ are sought by the iterative Newton-Raphson procedure,

$$(J) \begin{bmatrix} \Delta U_1^r - \Delta U_1^{r-1} \\ \Delta U_2^r - \Delta U_2^{r-1} \\ \vdots \\ \Delta U_{f-1}^r - \Delta U_{f-1}^{r-1} \\ \phi_1^r - \phi_1^{r-1} \\ \phi_2^r - \phi_2^{r-1} \\ \vdots \\ \phi_{f-1}^r - \phi_{f-1}^{r-1} \end{bmatrix} = - \begin{bmatrix} X_1^{r-1} \\ X_2^{r-1} \\ \vdots \\ X_{f-1}^{r-1} \\ X_f^{r-1} \\ X_{f+1}^{r-1} \\ \vdots \\ X_{2f-2}^{r-1} \end{bmatrix} \quad , \tag{43}$$

where J is the Jacobian,

$$J = J\left(\frac{x_1^{r-1}, \ x_2^{r-1}, \cdots, \ x_{2f-2}^{r-1}}{\Delta U_1^{r-1}, \cdots, \Delta U_{f-1}^{r-1}, \ \phi_1^{r-1}, \cdots, \ \phi_{f-1}^{r-1}}\right) \ . \tag{44}$$

Equation (43) gives an improved set of values for the variables ΔU and ϕ after r iterations in terms of values obtained from the $(r-1)^{st}$ iteration.

Inversion of the Jacobian matrix, equation (44), is the major computational task. The form of matrix J is shown in Figure 7, with non-zero elements indicated by Y's and A_i's. The Y's are, in general, different. Dashed lines divide J into square sub-matrices A, B, C and D:

$$J = \begin{bmatrix} A & B \\ C & D \end{bmatrix} \ . \tag{45}$$

The elements of matrices A and B are obtained in computations by analytical differentiation, while the elements of C and D are obtained primarily by numerical differentiation.

Equation (43) may be written more briefly as

$$\begin{pmatrix} A & B \\ C & D \end{pmatrix} \begin{pmatrix} \delta \Delta U \\ \delta \phi \end{pmatrix} = - \begin{pmatrix} X_U \\ X_\phi \end{pmatrix} \ , \tag{46}$$

where

$$\delta \Delta U \equiv \begin{bmatrix} \Delta U_1^r - \Delta U_1^{r-1} \\ \Delta U_2^r - \Delta U_2^{r-1} \\ \vdots \\ \Delta U_{f-1}^r - \Delta U_{f-1}^{r-1} \end{bmatrix} , \quad \delta \phi \equiv \begin{bmatrix} \phi_1^r - \phi_1^{r-1} \\ \phi_2^r - \phi_2^{r-1} \\ \vdots \\ \phi_{f-1}^r - \phi_{f-1}^{r-1} \end{bmatrix} ,$$

$$X_U \equiv \begin{bmatrix} x_1^{r-1} \\ x_2^{r-1} \\ \vdots \\ x_{f-1}^{r-1} \end{bmatrix} , \quad X_\phi \equiv \begin{bmatrix} x_f^{r-1} \\ x_{f+1}^{r-1} \\ \vdots \\ x_{2f-2}^{r-1} \end{bmatrix} \ . \tag{47}$$

Submatrix A is reduced to 1's on the diagonal and -1's on the super-diagonal by dividing each of the equations by A_i. Multiples of equations in A are then added to equations in C to reduce C to diagonal form. Those equations for which the diagonal element in C is non-zero are then divided through by this element, leaving C with 1's and 0's on the main diagonal and 0's off the main diagonal. Through all these operations the structures of B and D do not change. If there is a 0 in C(1,1), this is eliminated by adding the first equation in A and the second equation in C to the first equation in C. Other 0's along the C diagonal are replaced by 1's proceeding from the top of C to the bottom, by replacing X_{f-1+i} by

$$\left\{ X_{f-1+i} - X_{i-1} + X_{f-2+i} \right\} \quad , \tag{48}$$

it being understood that the X's, A's, B's, C's and D's involved are the current values obtained after all preceding operations. When this is completed C has become the identify matrix, I.

Equation (46) may then be written in the form

$$A(\delta\Delta U) + B(\delta\phi) = -X_U \tag{49}$$

$$I(\delta\Delta U) + D(\delta\phi) = -X_\phi . \tag{50}$$

Multiplying equation (50) through on the left by A and subtracting the result from (49) gives

$$(B - AD)(\delta\phi) = [-X_U + AX_\phi] . \tag{51}$$

This system of f-1 equations for $\delta\phi$ is solved taking advantage of the fact that (B-AD) has the same band structure as the original D matrix in Figure 7, plus one additional superdiagonal. The number of multiplications and divisions required is proportional to (f-1). Equation (49) for $\delta\Delta U$ is then readily solved, since A and B are both bi-diagonal.

D. Example Computations

With use of the equations in the preceding three sections and the Appendix, one may carry out computations for successive short time intervals to simulate the complete history of fluid movement in an arbitrary sequence of compactable units (e.g. shale) and permeable, non-compactable units (e.g. sand) beginning with their sedimentation. Units may be deposited in any order and at any rate. The history may include intervening time intervals with no deposition, or time intervals during which the topmost existing unit is eroded away at a specified rate. The pressure history in sand sections beneath shales may be dictated. Thus sands may be overpressured, normally pressured, or underpressured for their depth, with the result that they may become sources or sinks for waters migrating through shales. The deficit or excess water, as the case may be, is compensated by horizontal flow in the permeable sands. Alternatively one may specify that sand(s) between two shale units forms a lens, i.e., that the inflow, if any, is vertical and always equal to the vertical outflow. The bottom-most shale unit in a section is a special case. It may be required either that the shale be underlain by an impermeable unit or by a sand whose pressure history is dictated. Several types of shale units may be accommodated in the same section. Shale types are differentiated in terms of the physical characteristics (1) grain density, (2) dependence of permeability on porosity, and (3) dependence of porosity on matrix pressure and liquid limit or age. Thus, in the theory and computations 'shale' can mean any compressible lithology, such as shale, sand, silt, or chalk, which has a low, porosity-dependent permeability. Similarly 'sand' is used to connote any incompressible, very permeable lithology. A 'sand' is

specified by giving only its porosity and grain density. At the end of the
normal cycle of a sedimentary sequence, the pressure in the sand beneath one
particular shale may be arbitrarily decreased or increased as a function of
time to investigate the degree of flow of shale waters into or out of the sands.

Computational output consists of depth profiles at close time intervals
of (1) shale porosities, permeabilities, flow rates, compaction rates, unit
thicknesses, fluid pressure, matrix pressure and overburden pressure; and (2)
cumulative flows into and out of the tops and bottoms of all shale units in a
section. Only a small portion of the computed results can be shown in the
illustrations of this section, and only comparatively simple depositional
histories are dealt with in order to keep explanations brief.

Primary questions which need to be addressed in computations are:
'How large are the excess pressures which are produced as sediments accumulate?',
and 'How long do these pressures last, following deposition?'. These questions
are answered in Figures 8-21, which also show the influence of variations in rate
of deposition, depth of burial, geothermal gradient, permeability, liquid limit
or degree of shaliness, and boundary conditions. The 'standard' case illustrated
in these figures -- and also for Figures 22, 23, 25, and 26 -- is a shale with
(zero-porosity) thickness of 3000 m, liquid limit of 80 (=80 g water/100 g matrix),
permeability of 10^{-6} md at 20 percent porosity (Figure 6) and matrix density
2.77 g/cc. It is deposited on an impermeable base at the rate of 1 m of (zero
porosity) matrix per thousand years. The shale is buried beneath a normally
pressured sand of (zero porosity) thickness 3000 m, which has a porosity of 25
percent, a grain density of 2.66 g/cc, and is deposited immediately after the

shale at a rate of 1 m of (zero porosity) matrix per thousand years. The surface temperature is $20^{\circ}C$ and the geothermal gradient is $0.03^{\circ}C/m$ for all depositional, post-depositional, and erosional events. The pore water for sands and shales in all examples contains 60,000 ppm NaCl. In all figures for which thicknesses and depositional rates are posted, the reference is to meters of zero porosity matrix or grains. This convention is used because the actual thickness of the shale section generally varies as it compacts or de-compacts. Also during inelastic decompaction F=.5 (Figure 4 and Appendix). Unless otherwise mentioned or posted in the figures, these constants and conditions apply to all examples in Figures 8-29.

Profiles of porosity, of pressure in excess of normal pressure, of permeability, and of the velocity of water relative to the matrix are shown in Figure 22 for the standard case at 0, 10, and 100 million years subsequent to the deposition of the shale and sand.

An unexpected instability occurs if the standard case is altered by either (1) depositing and burying the shale more rapidly (Figure 8), (2) increasing the shale thickness (Figure 10), or (3) burying it deeper (Figure 12): Just below the top of the shale unit, as shown approximately by the arrows in Figure 22, the   pressure increases to the overburden, and the porosity increases to the porosity of a clay at the earth's surface. The explanation for this computed effect probably lies in the permeability-depth function. The permeability at the top of the shale during and just following sand-shale deposition is less than it is anywhere else in the shale (Figure 22). The shale is continuously compacting throughout, but water cannot get out of the top rapidly

enough, and so piles up in the depth region indicated by the arrows. This effect can occur when the shale-sand interface is at any sub-sea floor depth when depositional rates are very high. If this phenomenon were to happen in a real situation the high-porosity shales would have virtually no shear strength, and any perturbation would produce upward flow of the high porosity, low density shales. This may explain the origin of mud lumps, shale diapirs, and growth faults.

Figures 20 and 21 illustrate how the fluid pressure differs if instead of the standard case (a), the shale is deposited on a normally-pressured sand (b); or the shale is split by a 100 m sand with fluid pressure maintained by a lateral source at 95 percent of the overburden (c); or the shale is underlain by an additional 1500 m of shale (d); or the shale is overlain by 3000 m of shale instead or 3000 m of sand (e).

Figure 23 illustrates that for the shale split by the 100 m sand maintained at high fluid pressures (Figure 20C), there is a strong flow of water from the sand upward through the shale into the overlying 3000 m sand, but no downward flow because of the condition of impermeability at the shale base. For the shale underlain and overlain by normally pressured sands (Figure 20b) there is flow into both sands from the shale.

Figure 24 illustrates compaction of 375 m thick shales above and below a 100 m sand when the water pressure in the sand -- which had been maintained throughout the sedimentation history at 85 percent of the overburden by a lateral source -- is steadily decreased by 2000 psi (138 bar) over 180,000 years. During the pressure decline in the sand, the flow upward through the upper shale declines, while the flow from the lower shale upward into the sand increases.

In this example the upper and lower sands were deposited at the rate of 0.25 m/1000 yr, and have permeabilities of 10^{-4} md at 20 percent porosity. The intervening 100 m sand was deposited at a rate of 1.56 m/1000 year, and the upper 1500 m sand was deposited at a rate of 1 m/1000 years. Following deposition of the shale-sand-shale-sand sequence, a time lapse of 0.2 million years preceded the pressure decline in the sand between the shales.

Figure 25 illustrates how the porosity, excess pressure, and water velocity relative to the matrix vary in the standard shale as the normally-pressured overburden is removed at a rate of 1 m/1000 yr. Water begins to flow into the top of the shale -- i.e. the shale decompacts -- as erosion proceeds. At times, the bottom portion of the shale may be still compacting as the top decompacts. Also water pressure less than normal may exist in the upper portions of the shale while pressures are above normal in the lower portions. When, during the erosion process, any portion of the shale begins to experience matrix pressures less than the maximum previously experienced, it begins to decompact inelastically, i.e., F changes from 1 to 0.5 (Figure 2 and Appendix). For contrast, the conditions within the same shale after being exhumed are also illustrated for the case that it could decompact completely (F=1).

This example is continued in Figure 26 with the re-burial of the exhumed inelastic shale beneath 3000 m of the identical shale at a rate of 1 m/1000 yr. Discontinuities in porosity and flow occur at the unconformity. They are accentuated by the fact that the newly deposited shale is much more permeable than the older unit, and re-compacts the older unit just as a sand would. The porosity discontinuity at the unconformity produces a seismic reflector due to resulting density and velocity differences. The reflection coefficients at the

three interfaces shown are 0.11, 0.11, and 0.08. The reflector will mark the unconformity, even though the two shales as deposited were identical, until the top of the lower shale again experiences a matrix pressure equal to or greater than any previously experienced. Of course permanent porosity discontinuities and hence permanent reflectors are produced if shales with different liquid limits are deposited one on top of the other (Figure 2). Dallmus (1958) has documented several examples from Venezuela in which there is a sharp increase in shale density at an unconformity. There is too much scatter in the data to tell if there is a sharp density **maximum** at the unconformity, such as is predicted here. In a study of differential compaction of shales over and around Devonian reefs, O'Connor and Gretener (1974) have also shown shales below an unconformity to be more compacted than younger shales above the unconformity. Reflectors at shale-shale unconformities help explain the observation by Vail, Todd, and Sangree (1977) that seismic reflectors tend to follow time lines rather than interfaces between different lithologies.

Figures 27-29 illustrate the behavior of shales for which the porosity dependence on the matrix pressure and the sediment age is shown in Figure 5 and equation A6 of the Appendix. In Figures 27 and 28 a 3000 m shale is deposited, followed by a 2250 m sand. The excess fluid pressures are unusually large for this case because the grain-to-grain supporting forces decrease with sediment age, leaving more of the overburden to be supported by pore water pressure. The maximum excess pressure declines slowly after deposition but in this example actually begins to increase some time between 10 and 20 million years following deposition (Figure 28).

Figure 29 illustrates a 3000 m shale being re-buried beneath an identical but 'new' shale following an 111 million year history including deposition (3 million years), burial beneath a 3000 m sand (96 million years), and erosion of the overlying sand (12 million years). Here again there are discontinuities in the porosity and hence in the water velocity at the unconformity. The unconformity is a seismic reflector because of the density and velocity differences which result from the porosity differences. The porosity discontinuity and thus the reflector at the unconformity for this type shale never disappears entirely with increasing burial depth or time, because the age difference between the older and younger shale always exists. Computed reflection coefficients are 0.45, 0.46, and 0.42 at progressively deeper boundaries in Figure 29.

COMPACTION BY INTRUDING BODIES

Crosby (1965a, b) has inferred from a study of gravity data, in conjunction with well information, that the sedimentary strata along the flanks of piercement salt structures tend to be locally more dense than similar sediments at the same depth some distance away. He hypothesizes that there is a horizontal component of movement and local compaction of the sediments, particularly shales, to accommodate the dome as the salt shoulders its way toward gravitational equilibrium near the surface. This type of local compaction might also be expected adjacent to mudstone intrusives and igneous dikes.

In the example cited it should be possible, using the relationship among the porosity, overburden and pore fluid pressure of Figure 2 and the Appendix, to make estimates of the effective combined stress of the overburden and the salt, and to make estimates of what maximum fluid pressures might have

been produced in the shales by a sudden salt movement. These estimates would require determinations of porosity, fluid pressure, and overburden of equivalent shales both close to and distant from the intruding body.

OSMOTIC PRESSURES

If the water in a sedimentary section contains 35,000 ppm sodium chloride down to a given depth and is normally pressured, and if the temperature-depth relation is the same as for the compaction examples, it is required to compute the pressure in a sand lens 5 m deeper, the lens containing pore water of any given salinity and being enclosed in a rock type which will allow passage of water but not salt. Solutions to this problem are shown by solid lines in Figure 30 for a range of salinities in the lens of 0 to 250,000 ppm sodium chloride, and to depths of 6000 m (200°C). A set of solutions shown as broken lines in Figure 30 applies when the pore water in the section down to the depth in question contains 100,000 ppm sodium chloride. These results are sufficient to obtain with good accuracy the pressure difference between the water in the sand lens and the water in either (a) the upper section or, (b) another neighboring sand lens, for any assumed salinity in the upper section. For example at 6000 m Figure 30 gives the same pressure difference between a lens containing 250,000 ppm salt and a neighboring lens containing 0 ppm salt whether the salinity in the upper section is 35,000 ppm or 100,000 ppm.

All solutions are found by determining the pressure in the lens, P'', for which the sum of the partial molar Gibbs free energy, $\mu(T'',P'',N_s'')$, and the gravitational potential, gMZ'', of the water in the lens equals the sum of the

partial molar Gibbs free energy, $\mu(T',P',N_s')$, and the gravitational potential, gMZ', of the water in the sands above the semi-permeable rock type:

$$\mu(T'',P'',N_s'') + gMZ'' = \mu(T',P',N_s') + gMZ' \qquad (52)$$

Here T is the temperature, N_s is the salinity in moles of sodium chloride per liter, g is the gravitational acceleration, M is the molecular weight of water, and Z is the vertical distance above some arbitrary depth point. The super-scripts ' and " distinguish variables referring to the two sands. Each μ in equation (52) has been evaluated in the same way as a sum of three terms (Gibbs, 1875, p. 146,154):

$$\mu(T,P,N_s) = \mu(T,P_0,0) + \int_{P_0}^{P_N} v_g(T,p)dp + \int_{P_N}^{P} v_\ell(T,p,N_s)dp \; . \qquad (53)$$

$\mu(T,P_0,0)$ is the Gibbs free energy of pure water for the given temperature and at the pressure, P_0, at which water and its vapor are at equilibrium. The first integral over the partial molar volume of water vapor, $v_g(T,p)$, corrects $\mu(T,P_0,0)$ to the value $\mu(T,P_s,N)$ for the partial molar Gibbs free energy of water of salinity N_s in equilibrium with its vapor at temperature T. The second integral over the partial molar volume of liquid water, $v_\ell(T,p,N_s)$ corrects $\mu(T,P_N,N_s)$ to the in-situ pressure, P. In computations $\mu(T,P_0,0)$ was obtained from the ASME Steam Tables (1967), P_N was obtained from Fabuss and Korosi (1966), v_g was estimated using virial coefficients from Dymond and Smith (1969), and v_ℓ was obtained by differentiating analytical expressions given by Rowe and Chou (1970). P" is the only unspecified variable in equation (53) when equation (52) is substituted into it, and was computed by an iterative procedure to give the results in Figure 30.

Examination of Figure 30 indicates that the fluid pressure in the lens may be much greater or less than the normal pressure. However the best candidate rock type for a semi-permeable membrane is a shale, and shales will allow some salt to pass through for many of the conditions envisioned in Figure 30. Shales will progressively exclude the chloride ion and other anions from the pore space, and hence become more impermeable to salt, as they possess a high cation exchange capacity, as the pore size decreases, and as the salinity decreases (Smith, 1977; Smits, 1969). Conversely shales with low exchange capacities, high porosities, and high salinities will allow salt as well as water to pass through. Thus none of the projected pressures in Figure 30 approaching or exceeding the overburden will be observed, because (1) the shale porosity (Figures 2,5) and hence permeability to water and salt will increase dramatically as the pore fluid pressure in the lens approaches the overburden pressure, and (2) the higher pressures are associated with the higher salinities. It is expected that pressures in the lens more than 25 percent above the normal pressure would be unusual. Abnormal pressures due to osmotic phenomena should dissipate with time due to the movement of water and some salt across the shale.

GENERATION OF GAS

Under certain conditions of temperature (e.g., Tissot, 1969), pressure, and catalytic environment, either solid or liquid organically-derived materials in sedimentary rocks may react to produce lower molecular weight hydrocarbons including methane. One approach to studying the maximum fluid pressures which might be produced by this mechanism is to suppose that just methane is generated

within a thick shale, and to suppose that it is generated in a time span very short compared to that required for any significant flow of water or gas out of the shale. If the initial number of moles of water per given volume of matrix is N_w, and if the number of moles of water after the organic reaction in the liquid (') and possible gas phases (") are given by N_w' and N_w'' respectively, then

$$N_w' + N_w'' = N_w \quad . \tag{54}$$

Similarly if the total moles of methane generated is N_m, we have

$$N_m' + N_m'' = N_m \quad . \tag{55}$$

The number of moles of salt in the liquid phase, N_s, does not change:

$$N_s' = N_s \quad . \tag{56}$$

If K_w is the experimentally known ratio of the mole fraction of water in the gas phase to the mole fraction of water in the liquid phase, we have by definition

$$\frac{N_w''}{N_w'' + N_m''} = K_w \frac{N_w'}{N_w' + N_m' + N_s'} \quad . \tag{57}$$

Similarly, for methane,

$$\frac{N_m''}{N_w'' + N_m''} = K_m \frac{N_m'}{N_w' + N_m' + N_s'} \quad . \tag{58}$$

The ratios K_m and K_w are known as a function of temperature, pressure, and salinity (Culberson and McKetta, 1951; McKetta and Wehe, 1958).

The moles of methane produced, N_m, is given in terms of the density of the parent organic material, ρ_0, the volume, V_0, and the molecular weight of methane, M_m:

$$N_m = \frac{\rho_0 V_0}{M_m} \quad . \tag{59}$$

In computations suppositions must be introduced about ρ_0 and V_0. Hunt (1961) provides statistics on the weight, $\rho_0 V_0$, of organic materials found in shales. If the parent organic material is solid, and has been counted as matrix material rather than part of the pore fluid, the matrix volume is reduced from V_g to $V_g - V_0$ through the organic reaction. Void ratios in the shale before the organic reaction, e, and after e*, are

$$e = \frac{V}{V_g} \quad ,$$ (60)

and

$$e* = \frac{V'+V''}{V_g - V_0} \quad ,$$ (61)

where V and $V'+V''$ are the respective pore volumes before and after the production of methane. Each of these is related to the compaction history, the overburden (which is constant in this example), and to the pore fluid pressure through the relationship shown in Figure 2 and more fully in the Appendix. Thus,

$$e = e(S-p,F,\sigma_{max}) \quad ,$$ (62)

$$e* = e*(S-p*,F*,\sigma_{max}) \quad .$$ (63)

The pressure after the organic reaction, p*, may well be greater than that before. In that probable eventuality F* would be a fraction and not unity, so that the pressure p* would rise more rapidly than it would for F equal to unity.

Expressing the numerator in equation (61) as the sum of products of the moles, N, of each component in each phase with the partial molar volumes, v, of the corresponding quantities, we have

$$e*(S-p*,F*,\sigma_{max}) = \left(\frac{1}{V_g-V_o}\right) [N_w'v_w' + N_m'v_m' + N_s'v_s' + N_w''v_w'' + N_m''v_m'']$$ (64)

In the above expression N_w', N_m', N_s', N_w'' and N_m'' may be eliminated with use of equations (54)-(59). v_m' may be obtained from Kobayashi and Katz (1953). v_w' and v_s' may be obtained from Rowe and Chou (1970). v_w'' and v_m'' are functions of the virial coefficients (Dymond and Smith, 1969) and of temperature and pressure. With these visualized substitutions equation (64) becomes a function of the initial conditions such as composition, temperature, void ratio, and pressure; and of the final pressure, p*. It may therefore be solved for p*.

A problem not addressed in the above example is the solubility of methane in remaining organic material. This solubility, if taken into account, would probably have the effect of reducing p*.

As was the case for large osmotic pressures, the porosity and hence the permeability of the shales will increase with increasing p*, thus tending to limit p* in realistic situations. The increasing solubility of methane in water and the increasing density of any gas phase as p* increases will also help limit p*.

PORE SIZE DISTRIBUTIONS IN SHALES

Poiseuille's law indicates that the volume flow rate through a tube increases as the fourth power of the tube width, for a fixed pressure gradient. This result is insensitive to cross-sectional shape changes in the tube (Lamb,

1932, p. 587). Thus we feel that the major portion of the flow through a shale will be through the largest pores. This conclusion is supported by the existence of correlations of permeability with the threshold pressure for initiation of hydrocarbon flow through a water-wet core (Ibrahim, Tek, and Katz, 1970), as it is clear that, because the opposing capillary forces are least in the largest pores, hydrocarbons will enter these pores first. The largest pores not only permit the easiest passage for water and hydrocarbons, but also provide the easiest passage for dissolved salt, thus limiting the development and maintenance of osmotic pressures. For the above reasons investigations of the pore size distributions in shales, with the objective of understanding single or multi-phase flow in them, should take careful account of the larger pores.

Figure 31A illustrates the characterization of pore sizes in a Lower Tertiary shale of the North Sea basin as determined by mercury porosimetry. Also shown (Figure 31B) are proportional flow rates within successive incremental ranges of pore diameters. The proportional flow rates were computed from Poiseuille's law for tube bundles with the same pore size distribution as the shale. As already noted the proportional flow rates are insensitive to pore cross-sectional shape. This crude model is felt to be adequate to show that most of the flow should go through a small percentage of the pore space representing the largest pores.

Attempts to test the nature of these larger pores by varying the size of the sample injected with mercury led to the finding that progressively larger samples show progressively smaller percentages of pores more than a few times larger than the mode(s). An example of this type of test is shown in Figure 32. This

finding has been confirmed for many shales of differing geologic ages and geographic origins, and for various clay standards. The inference drawn is that most shales in situ do not have pores much larger than the mode. Pore size characterizations similar to those in Figure 31 are common in the literature (Heling, 1970, and Diamond, 1970) and have been used to guide theoretical studies of permeabilities and electrical conductivities, e.g., Madden (1976).

CONCLUSIONS

A complete theory of gravitational compaction of shale-sand sequences, utilizing a Lagrangian frame of reference tied to the matrix and adapted to a finite-difference method of solution using the Newton-Raphson technique, is presented in detail. Many situations of interest to geologists and geophysicists are illustrated graphically. The dependence of both excess pressure following deposition and the persistence of such excess pressures are shown as a function of sediment depositional rate, shale unit thickness, shale burial depth, geothermal gradient, shale permeability, shale liquid limit and permeability combined, and boundary conditions. Also shown are: variation of water flow rate and direction in shales subject to different boundary conditions; response of shales to decreasing water pressure in an overpressured sand; inelastic and elastic rebound of a shale during erosion; density discontinuities at unconformities resulting from re-burial of an exhumed inelastic shale under a similar shale; and excess pressures in a shale for which grain-to-grain restoring forces weaken with age. Unusual features of the predictions include: both compaction and decompaction occurring in the same shale unit simultaneously; pressures above and below normal occurring simultaneously in the same unit; a mechanism for

producing mud lumps and diapirs; an exaggerated low-porosity 'lip' at the top of an exhumed shale being buried beneath a similar shale; and an increase in pore fluid pressure with time, rather than a decrease, when grain-to-grain forces weaken with age. Reflection coefficients on the order of 0.1 to 0.5 are obtained for shale-shale unconformities. Computations use realistic permeabilities and compaction characteristics. Quantitative approaches to computing high pressures in shales due to gas generation and to stresses caused by nearby intrusives are discussed but no computations are made. Osmotic pressure computations are presented graphically for most situations of interest where ordinary salt is involved. Finally the importance of the largest pores in shales to migration of water, of hydrocarbons, and of salt is discussed, and previously accepted results using mercury porosimetry are challenged by showing that the proportion of pores larger than the mode declines radically as the shale sample size increases.

APPENDIX A

Skempton (1970) has given two graphical correlations for clays in sedimentary sections from which a relationship among the fractional porosity, ϕ, the matrix pressure, σ, and the clay liquid limit, LL, may be deduced. This will be carried out beginning with Skempton's Figures 5 and 22, which are shown in modified form in Figures 3 and 4 respectively. The dashed lines enclose Skempton's data, and the solid lines are our straight line approximations. Combining the straight line relationships in the two figures gives the water content, w, in terms of the liquid limit, LL, and the matrix pressure, σ:

$$w = (.23LL+12.4) + (.77LL-12.4)(.66-.175\ln\sigma) \tag{A1}$$

Porosity is related to w approximately by

$$\phi = \frac{.027w}{1+.027w} \quad , \tag{A2}$$

so that the two equations together give porosity as a function of matrix pressure and liquid limit. Water content, w, is defined as

$$w = 100 \left(\frac{\text{wt water in sample}}{\text{wt dry matrix in sample}} \right) . \tag{A3}$$

The value of w at which there is a transition from liquid to plastic behavior is the liquid limit. This may be determined experimentally from cores or cuttings.

Equation (A1) has been modified so that (1) w and ϕ go asymptotically to zero rather than to negative values as σ goes to infinity; (2) w and ϕ attain maximum, finite values rather than infinite values when $\sigma=0$, i.e., at the surface; and (3) the slope in the correlation in Figure 4 is multiplied by a fraction, F,

for matrix pressures less than the maximum experienced value, σ_{max}. The
resulting equation, which with equation (A2) is used in computations and
illustrated in Figure 2, is

$$w = (.23LL+12.4) + (.77LL-12.4)\left\{3.07-.175\ln B-.175(1-F)\ln\left[1-e^{-\frac{\sigma_{max}+100}{B}}\right]\right\}$$

$$- .175F(.77LL-12.4)\ln\left[1-e^{-\frac{\sigma+100}{B}}\right] \quad , \tag{A4}$$

with

$$B = e^{\frac{1}{.175}\left[3.07 + \frac{.23LL+12.4}{.77LL-12.4}\right]} \quad . \tag{A5}$$

This expression agrees with Skempton's data in the experimental range. In
equation (A4) and (A5) σ and B have units dyne/cm^2. The above correlation is
used in the computations for Figures 8-26.

A different correlation relating fractional porosity, matrix pressure,
and time since deposition of a sediment has been used in Figures 5 and 27-29:

$$\phi = .8e^{-.1(T+1.5)^{.23}(14.5\sigma)^{.25}} \quad . \tag{A6}$$

T is the sediment age in millions of years and σ is in bars. Equation A6
requires an explanation in that porosity is obviously not a function of sediment
age in a fundamental sense. Sediment age is used in the correlation to stand in
for diagenetic changes which do occur in shales over geologic time due to
pressure, temperature and chemistry of minerals and pore waters. Sediment age
is also used in the correlation for expediency, since it is often known. The
form of equation A6 was devised to agree jointly with Athy's (1930) porosity-
depth data for Permian and Pennsylvanian shales in north-central Oklahoma, and
with data for a 12000 ft offshore Texas well which penetrated Pleistocene
through Middle Miocene shales and sands. For the latter well the overburden

and porosity were estimated from the density log and the fluid pressure was
estimated from the sonic log using the Hottman-Johnson (1965) technique calibrated
with two deep wireline pressure tests. The form of the equation was also guided
by correlations by Faust (1950) and Pennebaker (1968) which show the sonic
velocities in sedimentary sections to increase systematically with depth and
age. Manger's (1963) literature survey of porosity data for shales also shows
a systematic decrease of porosity with both age and depth of burial. The
increasing availability of borehole gravimeter data will determine the dependence
of shale porosity on burial history and age in the near future.

ACKNOWLEDGMENTS

REFERENCES

1. Athy, L. F., 1930, Density, porosity, and compaction of sedimentary rocks: Bull. AAPG, v. 14, p. 1-24.

2. Bryant, W. R., Hottman, W., and Trabant, P., 1975, Permeability of unconsolidated and consolidated marine sediments, Gulf of Mexico: Marine Geotechnology, v. 1, p. 1-14.

3. Burst, J. F., 1969, Diagenesis of Gulf Coast clayey sediments and its possible relation to petroleum migration: Bull. AAPG, v. 53, p. 73-93.

4. Crosby, G. W., 1965a, Gravity anomaly and salt dome elongation in the lower Gulf Coast salt basin: paper presented SEG 35th meeting, Dallas, Texas.

5. Crosby, G. W., 1965b, Compaction halo surrounding Gulf Coast salt domes: Geol. Soc. America, Special Paper 82.

6. Culberson, O. L., and McKetta, J. J. Jr., 1951, Phase equilibria in hydrocarbon-water systems-IV: Trans. AIME, v. 192, p. 297-300.

7. Dallmus, K. F., 1958, Mechanics of basin evolution and its relation to the habitat of oil in the basin: in Habitat of Oil, L. G. Weeks, editor: Tulsa, Amer. Assoc. Petrol. Geol., p. 883-931.

8. Diamond. S., 1970, Pore size distributions in clays: Clays and Clay Minerals, v. 18, p. 7-23.

9. Dymond, J. H., and Smith, E. B., 1969, Virial coefficients of gases, Clarendon, Oxford U. Press.

10. Fabuss, B. M. and Korosi, A., Properties of sea water and solutions containing sodium chloride, potassium chloride, sodium sulfate and magnesium sulfate: OSW R&D Prog. Rep. No. 384, Washington, U.S. Gov't. Ptg. Off.

11. Faust, L. Y., 1950, Seismic velocity as a function of depth and geologic time: Geophysics, v. 16, p. 192-206.

12. Gambolati, G., Gatto, P. and Freeze, R. A., 1974, Mathematical simulation of the subsidence of Venice, part 2, results: Water Resources Research, v. 10, p. 563-577.

13. Gibbs, J. W., 1875, On the equilibrium of heterogeneous substances: in Scientific Papers of J. Willard Gibbs, v. 1, p. 55-371: New York, Dover Publ., Inc.

14. Gretener, P. E., 1969, Fluid pressure in porous media - its importance in geology: a review: Bull. Can. Petrol. Geol., v. 17, p. 255-295.

15. Heling, D., 1970, Micro-fabrics of shales and their rearrangement by compaction: Sedimentology, v. 15, p. 247-260.

16. Helm, D. C., 1980, Conceptual aspects of subsidence due to fluid withdrawal: in press as Geol. Soc. Amer. Special Paper in Recent trends in hydrogeology: edited by T. N. Narasimhan and R. A. Freeze.

17. Hottman, C. E., and Johnson, R. K., 1965, Estimation of formation pressures from log-derived shale properties: Trans. Gulf Coast Assoc. of Geol. Soc., v. 15, p. 179-186.

18. Hunt, J. M., 1961, Distribution of hydrocarbons in sedimentary rocks: Geochimica et Cosmochimica Acta, v. 22, p. 37-49.

19. Ibrahim, M. A., Tek, M. R., and Katz, B. L., 1970, Threshold pressure in gas storage: Amer. Gas. Assoc. Inc., Arlington.

20. Kobayashi, R. and Katz, D. L., 1953, Vapor-liquid equilibria for binary hydrocarbon-water systems: Indus. and Eng. Chem., v. 45, p. 440-451.

21. Lamb, H., 1932, Hydrodynamics, Sixth Ed.: New York, Dover Publ. Inc.

22. Madden, T. R., 1976, Random networks and mixing laws: Geophysics, v. 41, p. 1104-1125.

23. Manger, G. E., 1963, Porosity and bulk density of sedimentary rocks: USGS Bull. 1144-E, 55 pp.

24. McKetta, J. J. Jr., and Wehe, A. H., 1958, Use this chart for water content of natural gasses: Hydrocarbon Processing and Petroleum Refiner, August 1958, p. 153-154.

25. Neglia, S., 1979, Migration of fluids in sedimentary basins: AAPG Bull., v. 63, p. 573-597.

26. O'Conner, M. J., and Gretener, P. E., 1974, Differential compaction within the Woodbend Group of Central Alberta: Bull. Can. Petrol. Geol., v. 22, p. 269-304.

27. Pennebaker, E. S., 1968, An engineering interpretation of seismic data: Soc. Petrol. Eng. paper 2165 presented at SPE 43rd Annual Fall Meeting, Houston, Sept. 29-Oct. 2.

28. Rowe, A. M. and Chou, J. C. S., 1970, Pressure-volume-temperature-concentration relation of aqueous NaCl solutions: J. Chem. Eng. Data, v. 15, p. 61-66.

29. Skempton, A. W., 1970, The consolidation of clays by gravitational compaction: Quart. J. of Geol. Soc. (London), v. 125, p. 373-341.

30. Smith, J. E., 1971, The dynamics of shale compaction and the evolution of pore fluid pressures: J. Internat. Assoc. Math. Geol., v. 3, p. 239-263.

31. Smith, J. E., 1973, Shale compaction: Soc. Petrol. Eng. J., Feb. 1973, p. 12-22, and Trans. AIME, v. 255, p. 12-22.

32. Smith, J. E., 1977, Thermodynamics of salinity changes accompanying compaction of shaly rocks: Soc. Petrol. Eng. J., Oct. 1977, p. 377-386.

33. Smits, L. J. M., 1969, Proprietes electrochimiques de sables argileux
     et de schistes argileux: Revue De L'Institut Francais Du Petrole, v. 24,
     no. 1, p. 91-120.

34. Tissot, B., 1969, Les mechanismes et la cinetique de la formation du
     petrole dan les sediments: Revue De L'Institut Francais Du Petrole, v. 24,
     p. 470-501.

35. Verwey, E. J. W., and Overbeek, J. Th. G., 1948, Theory of the stability
     of lyophobic colloids: Amsterdam, Elsevier Publ. Co., Inc.

36. Vail, P. R., Todd, R. G., and Sangree, J. B., 1977, Chronostratigraphic
     significance of seismic reflections, in C. E. Payton, ed., Seismic
     stratigraphy-applications to hydrocarbon exploration: Tulsa, AAPG
     Memoir 26, p. 99-116.

TABLE 1
EQUATIONS FOR FINITE DIFFERENCE METHOD

ASSOCIATED VARIABLE	X SUBSCRIPTS	EQUATIONS
$\Delta U_a \rightarrow \Delta U_{b-1}$	$X_a \rightarrow X_{b-1}$	$0 = \int_{U_k}^{U_{k+1}} (1-\Phi)dZ - R_k, \quad a \leq k \leq b-1$
ΔU_b	X_b	$0 = \Delta U_b - \Delta U_{b+1} - \underset{*}{\Sigma} H$ ($0 = \Delta U_f$, IF UNIT ℓ IS THE TOPMOST SHALE UNIT IN THE SECTION)
Φ_a	X_{f-1+a}	(A) IMPERMEABLE BASE: $0 = \left[\frac{K}{\eta} \frac{\partial}{\partial Z} \left\{ g \int_{Z_{sw}}^{Z} (\rho_g - \rho_w)(1-\Phi)\, dZ + \sigma \right\} \right]_a$ (B) UNDERLYING SANDS FORM A LENS: $0 = \left[\frac{K}{\eta} \frac{\partial}{\partial Z} \left\{ g \int_{Z_{sw}}^{Z} (\rho_g - \rho_w)(1-\Phi)\, dZ + \sigma \right\} \right]_a - \left[\frac{K}{\eta} \frac{\partial}{\partial Z} \left\{ g \int_{Z_{sw}}^{Z} (\rho_g - \rho_w)(1-\Phi)\, dZ + \sigma \right\} \right]_{a-1}$ (C) DICTATED P_a: $0 = \sigma_a - (1-\alpha_\ell) g \int_{U_a}^{Z_{sw}} (\rho_g - \rho_w)(1-\Phi)\, dZ - (1-\beta_\ell)(g\rho_w)(\Delta U_a + \underset{**}{\Sigma} H)$
$\Phi_{a+1} \rightarrow \Phi_{b-1}$	X_{f-1+k} $a+1 \leq k \leq b-1$	$0 = \left[\frac{K}{\eta} \frac{\partial}{\partial Z} \left\{ g \int_{Z_{sw}}^{Z} (\rho_g - \rho_w)(1-\Phi)\, dZ + \sigma \right\} - \frac{d\Delta U}{dt} \right]_k - \left[\frac{K}{\eta} \frac{\partial}{\partial Z} \left\{ g \int_{Z_{sw}}^{Z} (\rho_g - \rho_w)(1-\Phi)\, dZ + \sigma \right\} - \frac{d\Delta U}{dt} \right]_{k-1}$
Φ_b	X_{f-1+b}	$0 = \sigma_b - \sigma_{b+1} - (\underset{*}{\Sigma} g (\rho_g - \rho_w)h)$ ($0 - \sigma_f$)

* SUM OVER ALL SAND UNITS BETWEEN SHALE UNITS ℓ AND $\ell+1$

** SUM OVER ALL SAND UNITS, IF ANY, OVERLYING THE TOPMOST EXISTING SHALE UNIT IN THE SECTION

σ IS A FUNCTION OF Φ, F, AND σ_{MAX} IF SKEMPTON'S CORRELATION IS USED.

SHALE NODE
NUMBER

SHALE UNIT
NUMBER

$f = 19$

18

$\Big\}$ 4

17

(SAND)

(SAND)

16

15

14

$\Big\}$ 3

13

12

11

10 — — — — — — — — — — $Z = U_{10}$

9 $\Big\}$ 2

8

(SAND)

7

6

5

Z AXIS

4

3

1

2

1 $Z = 0$
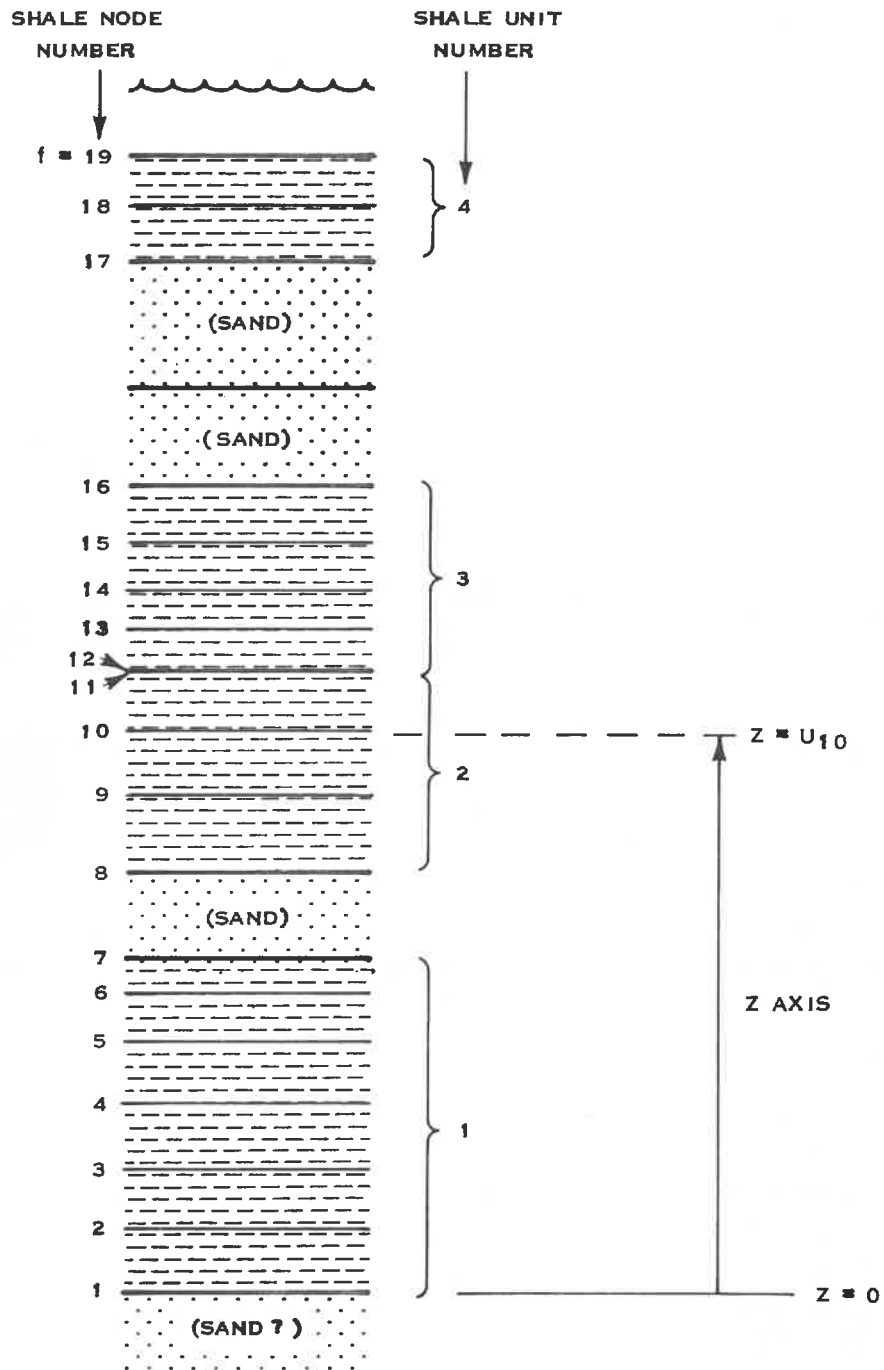
(SAND ?)

FIGURE 1
SEDIMENTARY COLUMN SHOWING COORDINATE SYSTEM
AND NUMBERING SYSTEM FOR SHALE UNITS AND NODES
WITHIN SHALES.
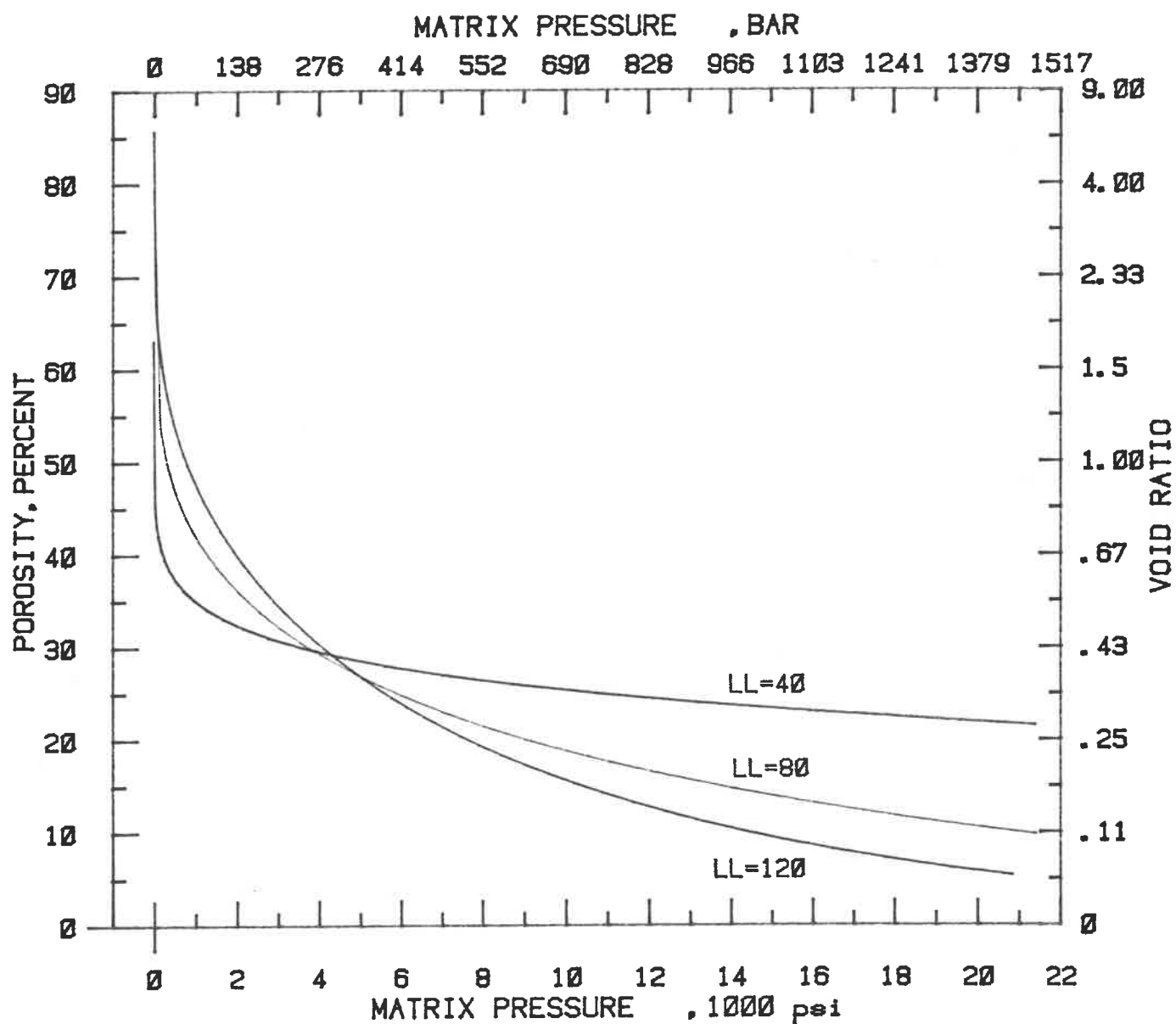
Figure 2. Porosities as a function of matrix pressure and liquid limit, based on Skempton's (1970) correlations
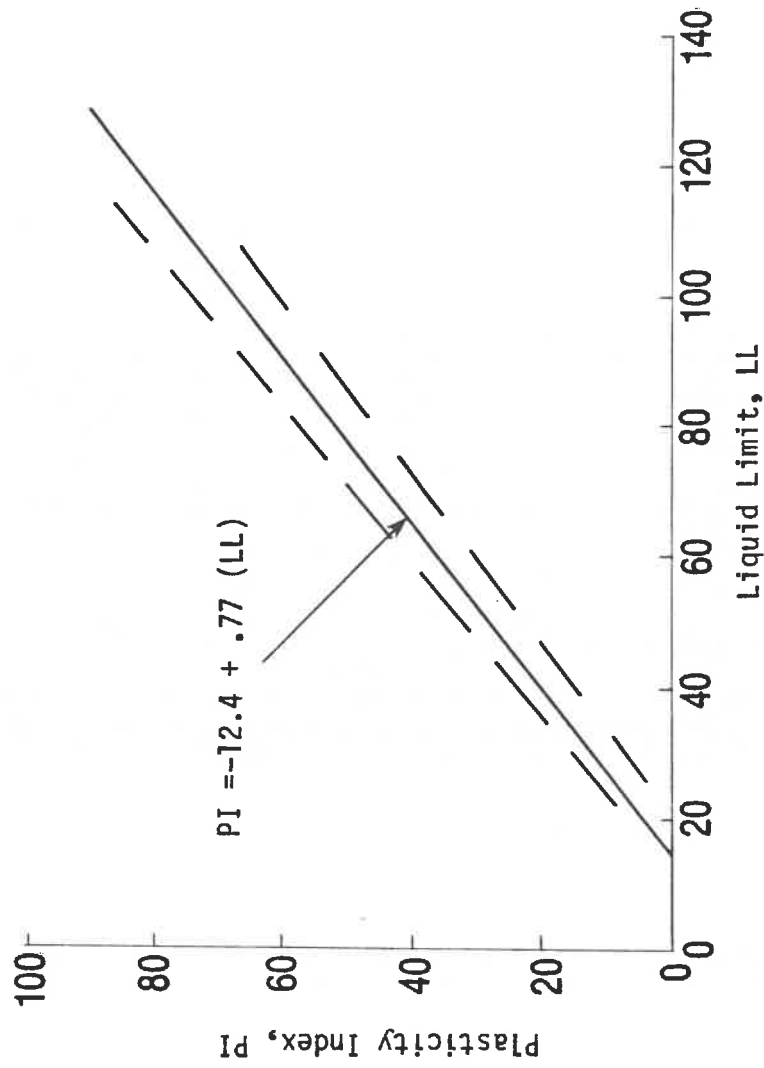
FIGURE 3 - Straight line approximation to Skempton's (1970) correlation of plasticity index and liquid limit.
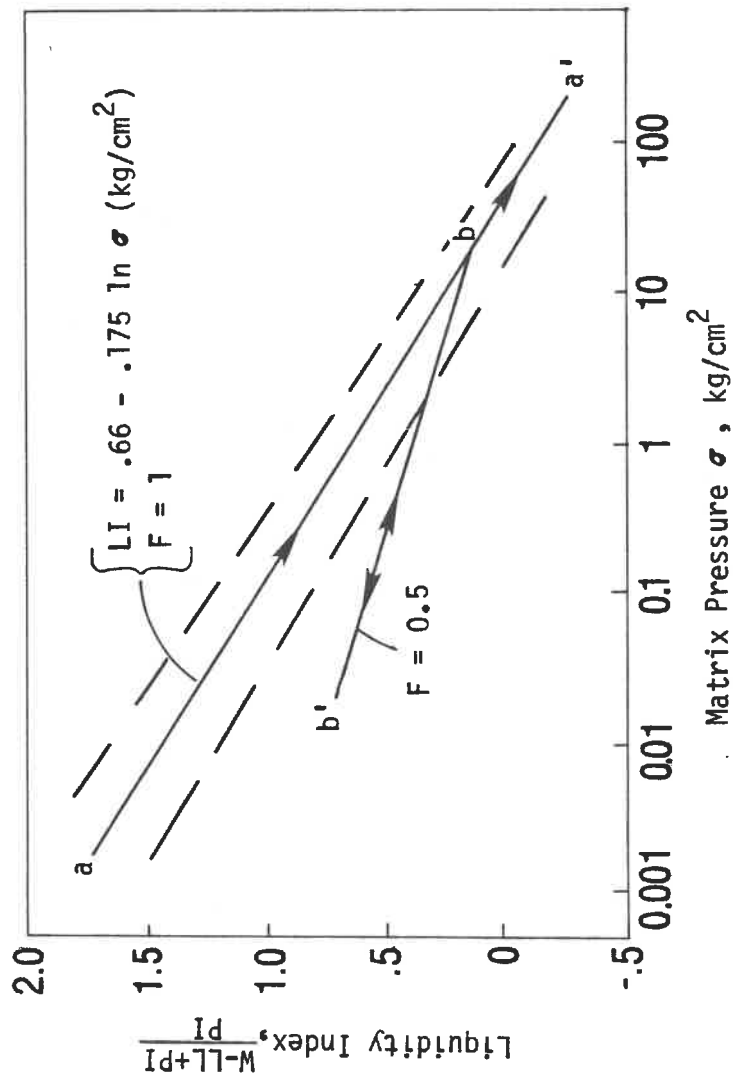
FIGURE 4 – Straight line approximation a–a' to Skempton's (1970) correlation of liquidity index to matrix pressure. Upon unloading clay at b, decompaction occurs along b–b' for which the slope is a fraction, F, of the original compaction curve, a–a'.
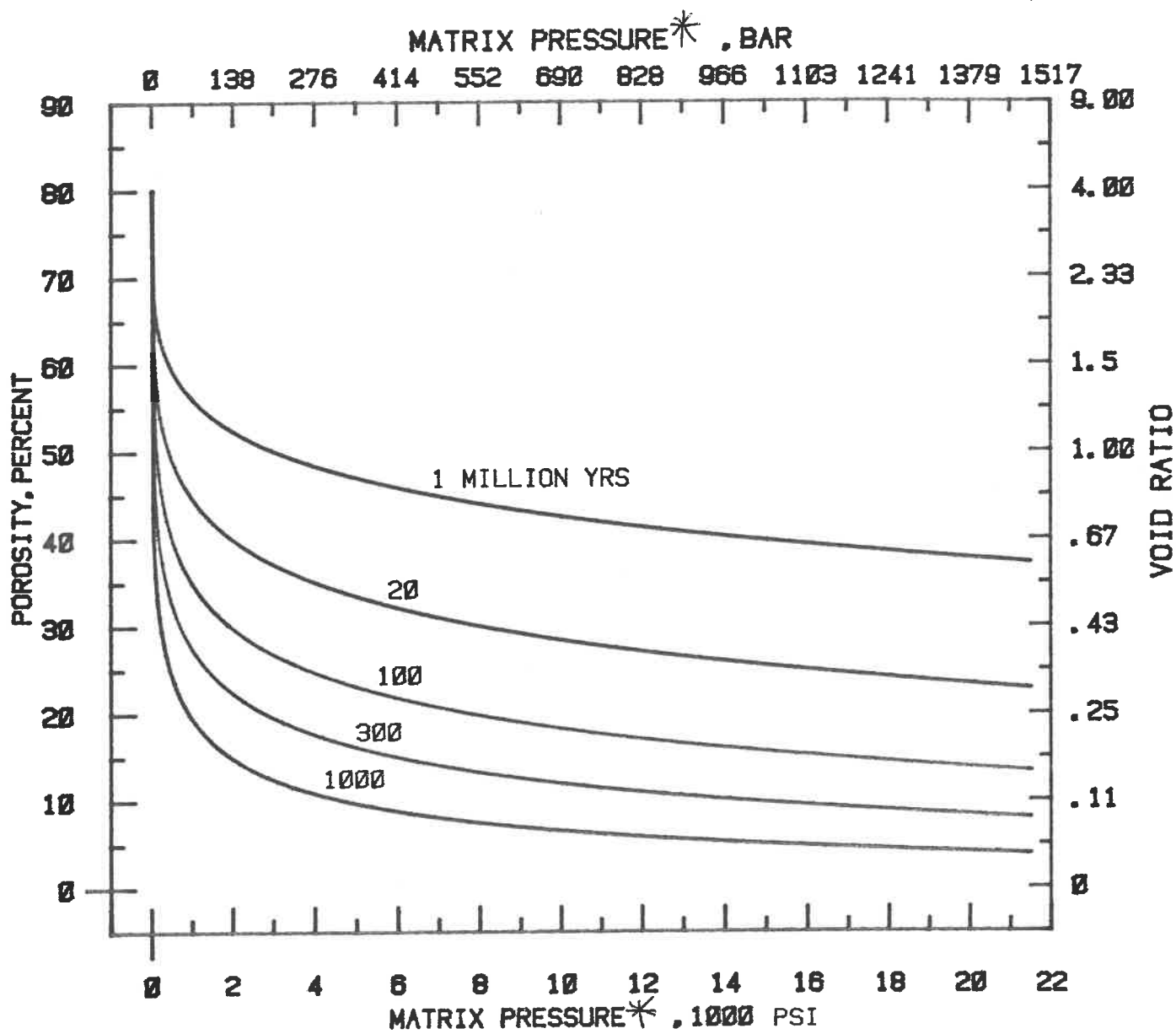
Figure 5 Apparent dependence of porosity on matrix pressure and geologic age.

$\left(* \text{ Divide numbers on axes by } 14.5 \right)$

FIG. 6 DEPENDENCE OF PERMEABILITY ON THE EIGHTH POWER OF THE POROSITY.

FIGURE 7

JACOBIAN MATRIX FOR SEDIMENTARY SECTION SHOWN AT RIGHT
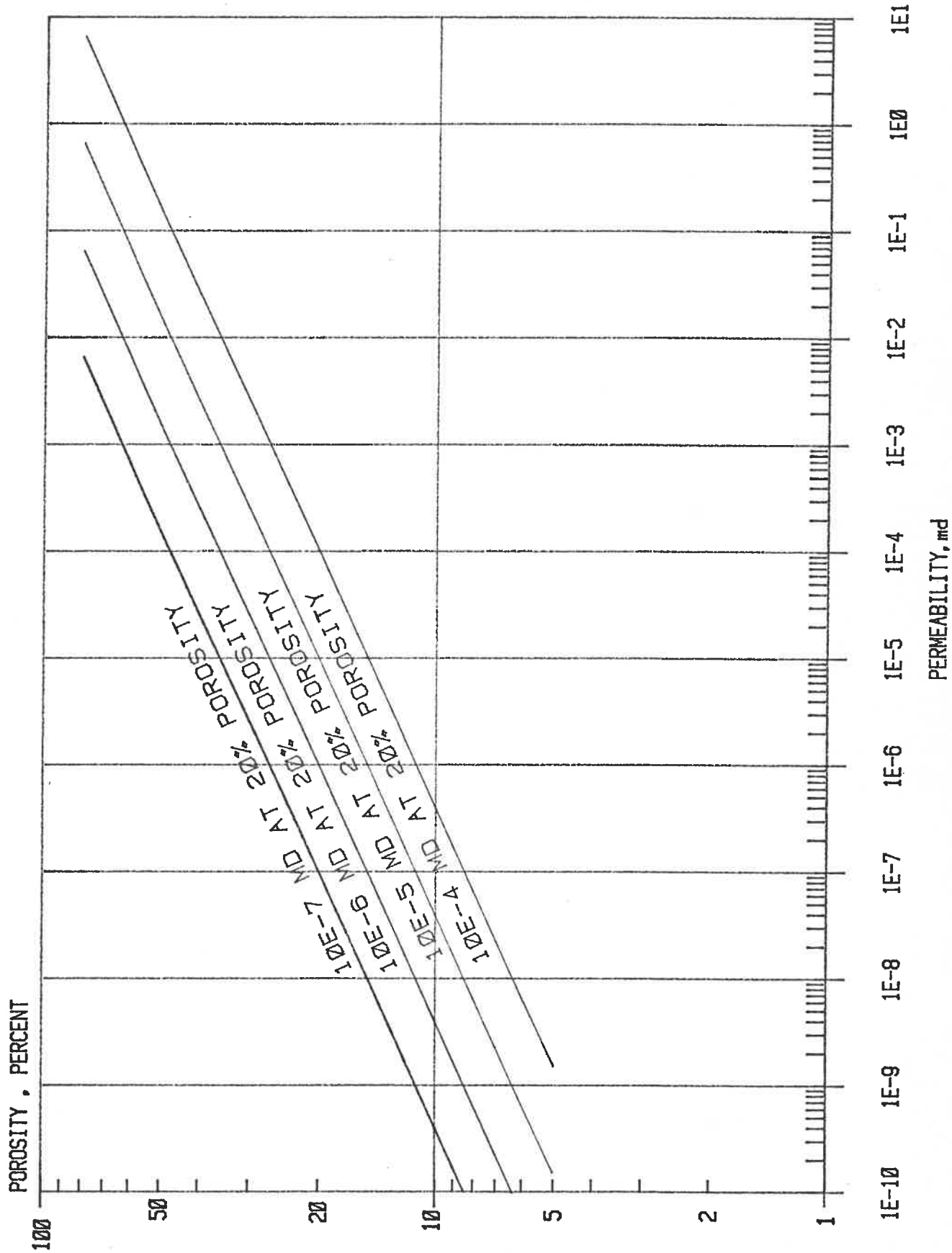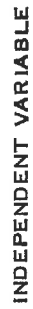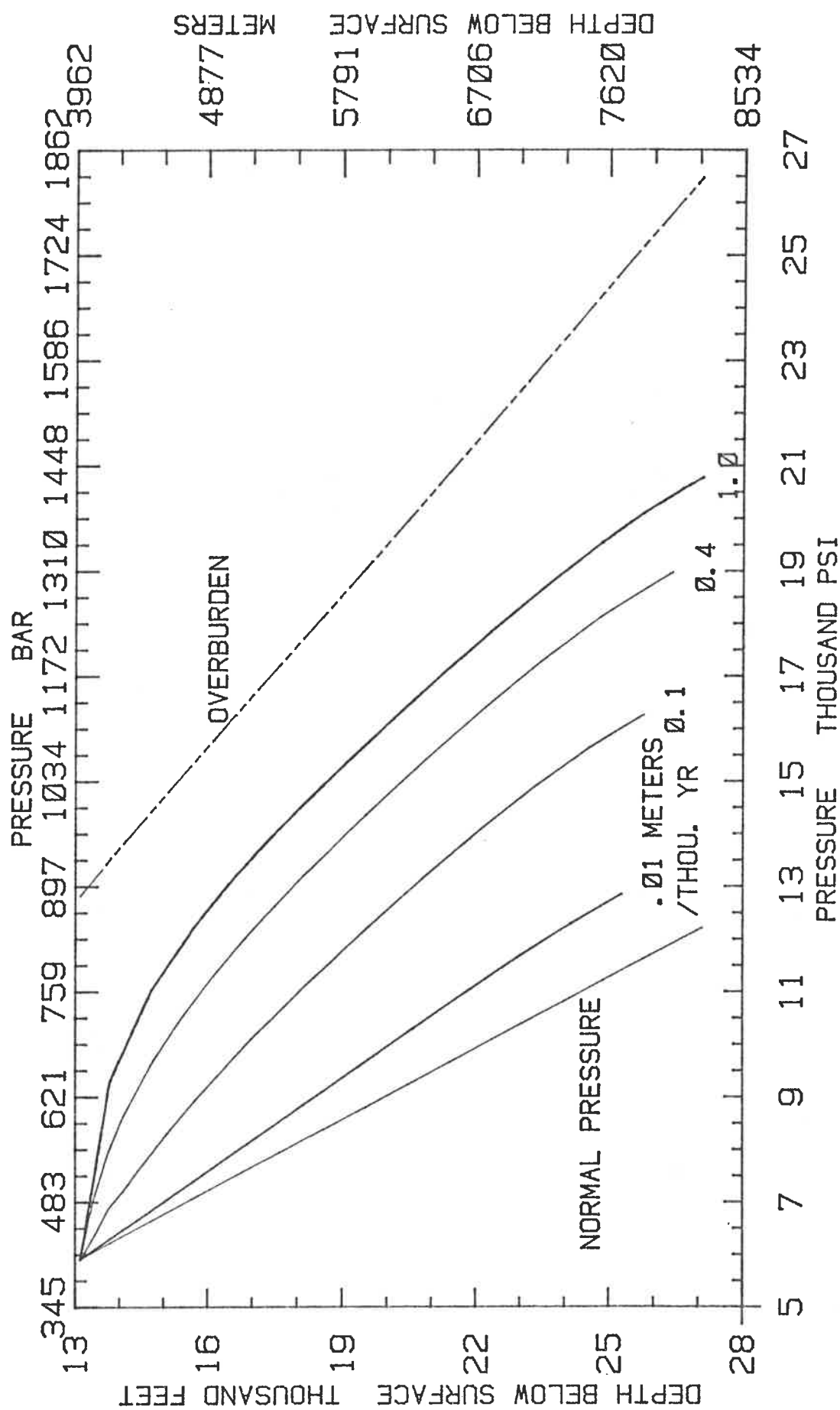
FIGURE 8   EFFECT OF DEPOSITIONAL RATE ON THE FLUID PRESSURES IN THE
SHALE UNIT IMMEDIATELY FOLLOWING DEPOSITION OF THE
SHALE-SAND SEQUENCE
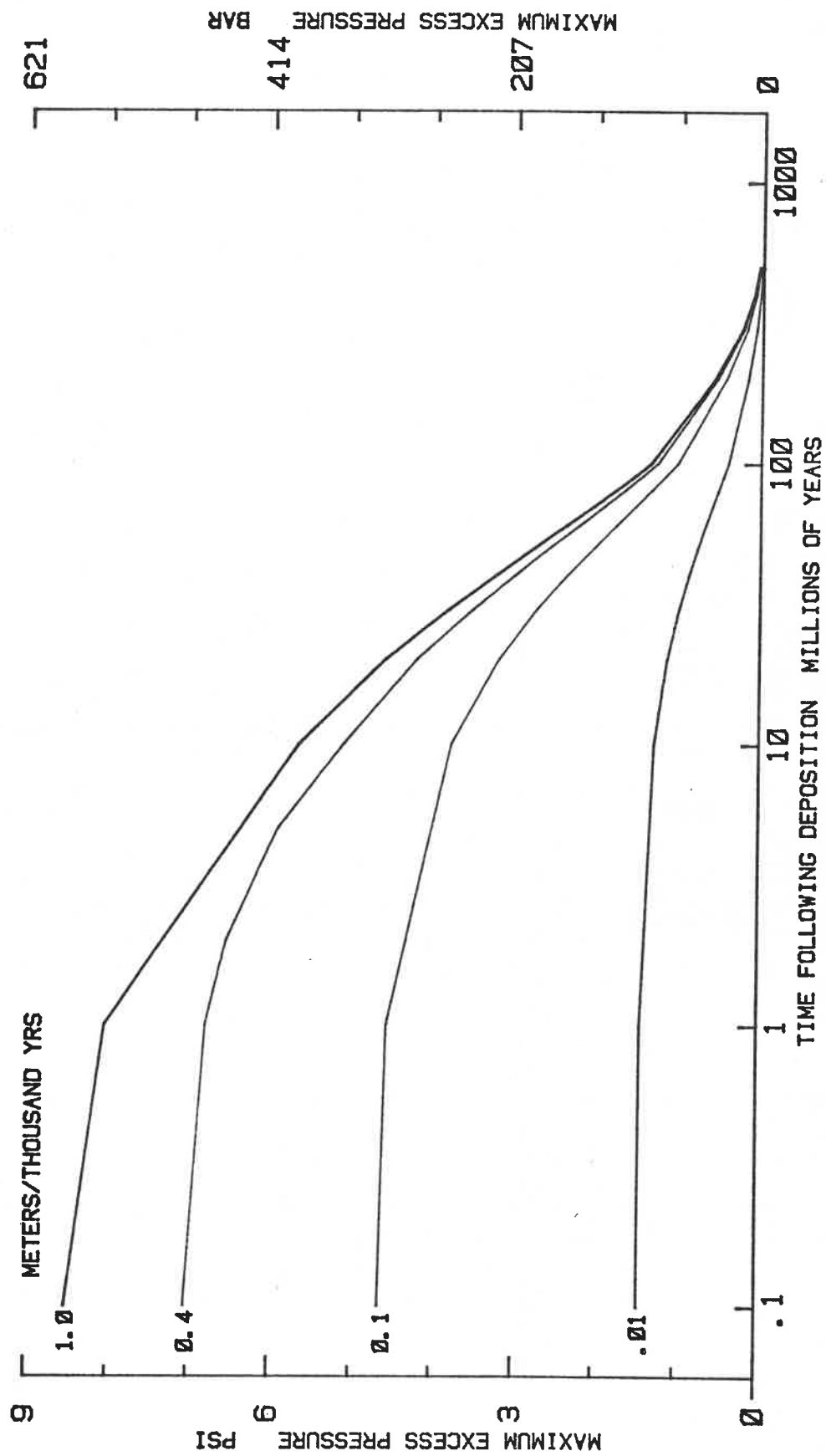
FIGURE 9 PERSISTENCE OF ABNORMAL FLUID PRESSURES FOLLOWING DEPOSITION OF SAND-SHALE SEQUENCE AT SEVERAL RATES.
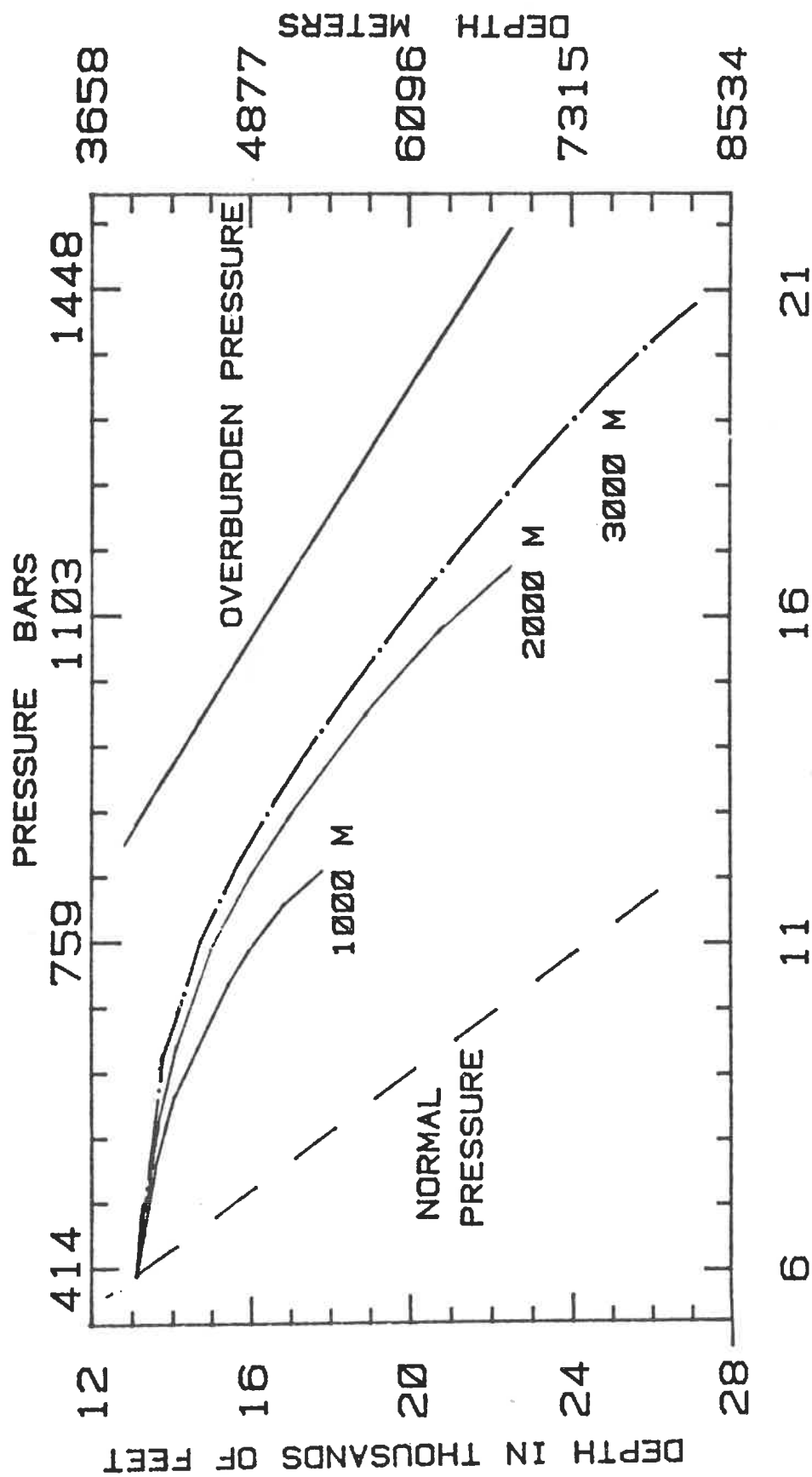
FIG. 10 INFLUENCE OF SHALE THICKNESS ON EXCESS PRESSURE
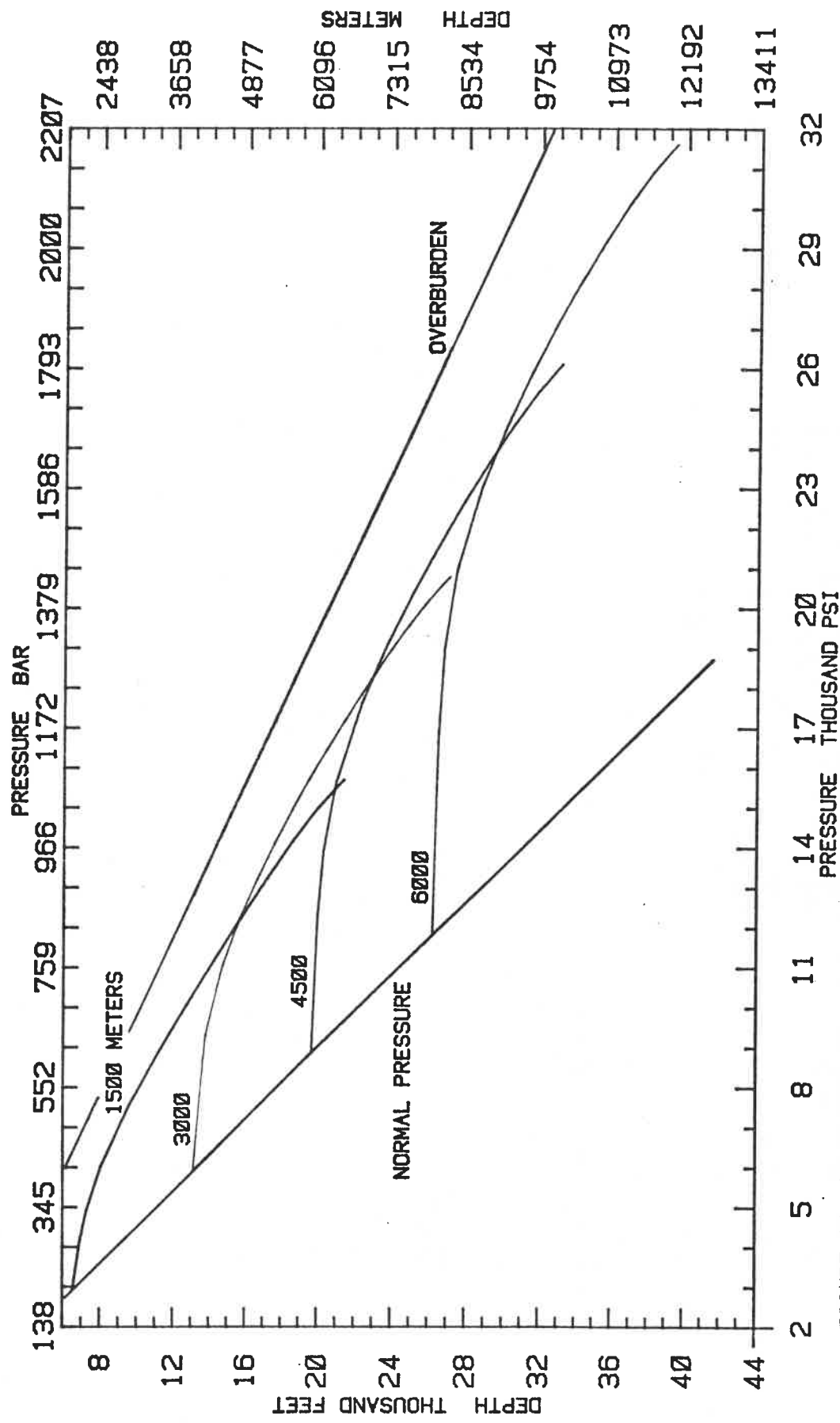
FIGURE 12 INFLUENCE OF BURIAL DEPTH ON EXCESS PRESSURE IN A SHALE
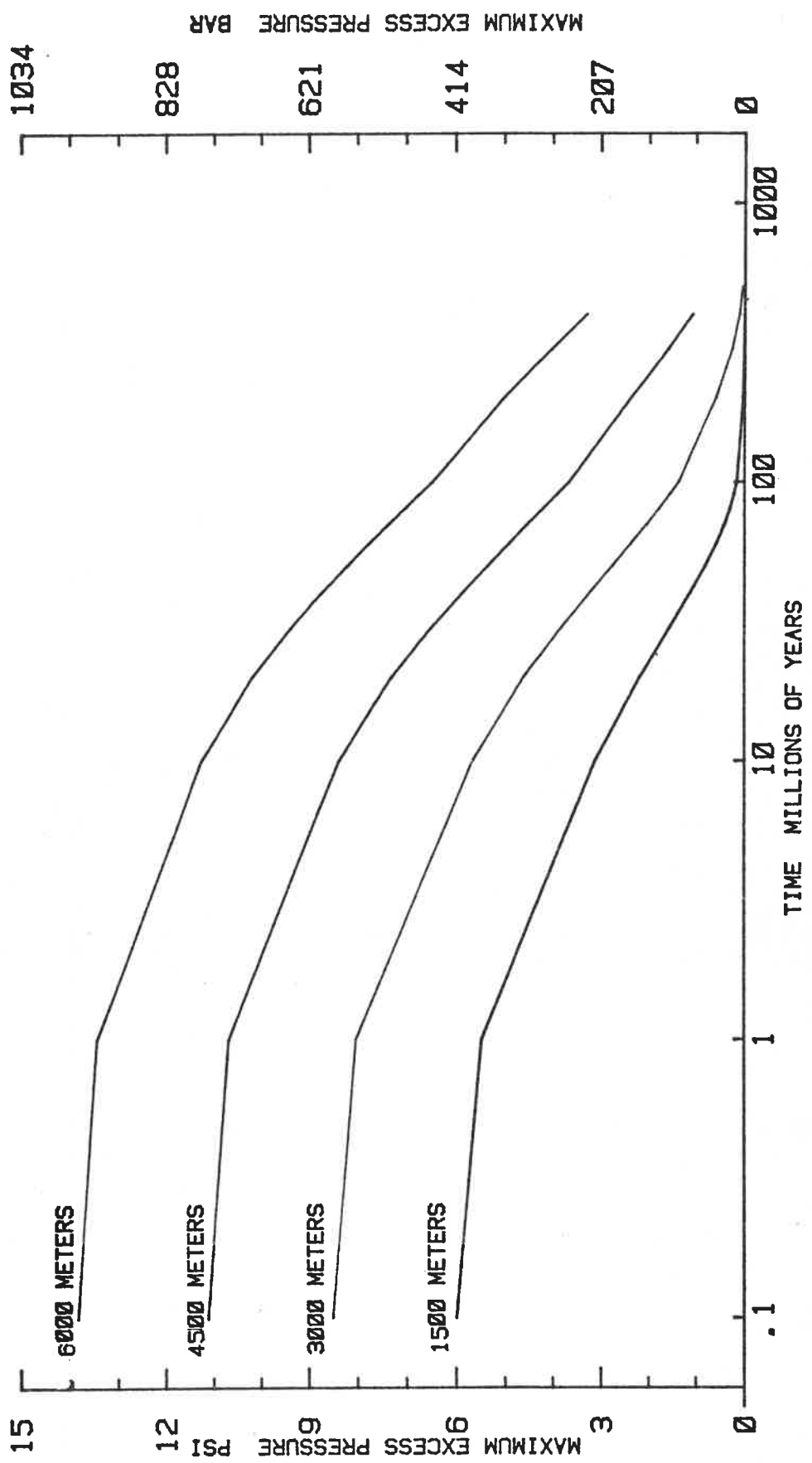
FIGURE 13   INFLUENCE OF DEPTH OF BURIAL OF SHALE
ON PERSISTENCE OF EXCESS PRESSURE
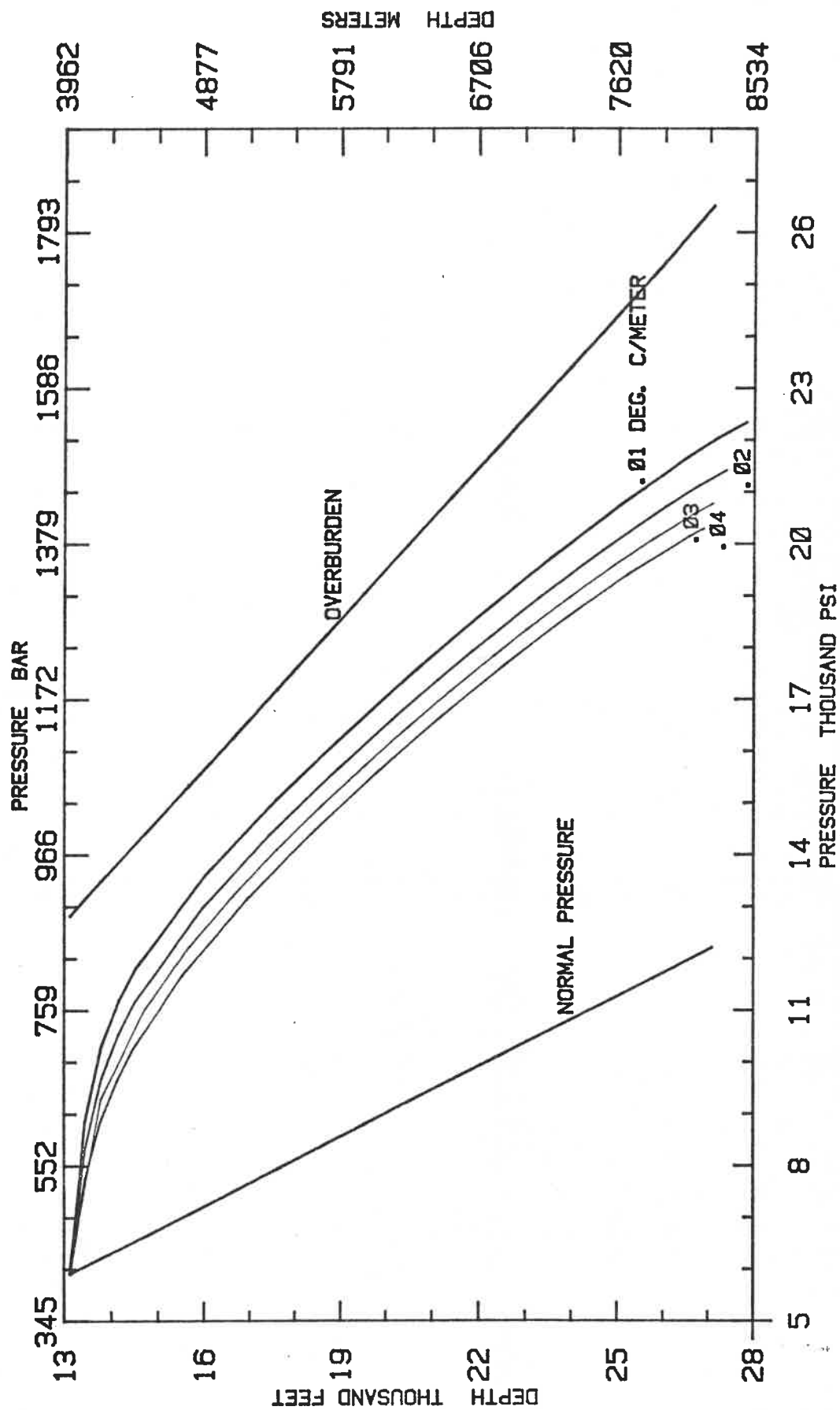
FIGURE 14 INFLUENCE OF GEOTHERMAL GRADIENT ON EXCESS PRESSURE IN A SHALE
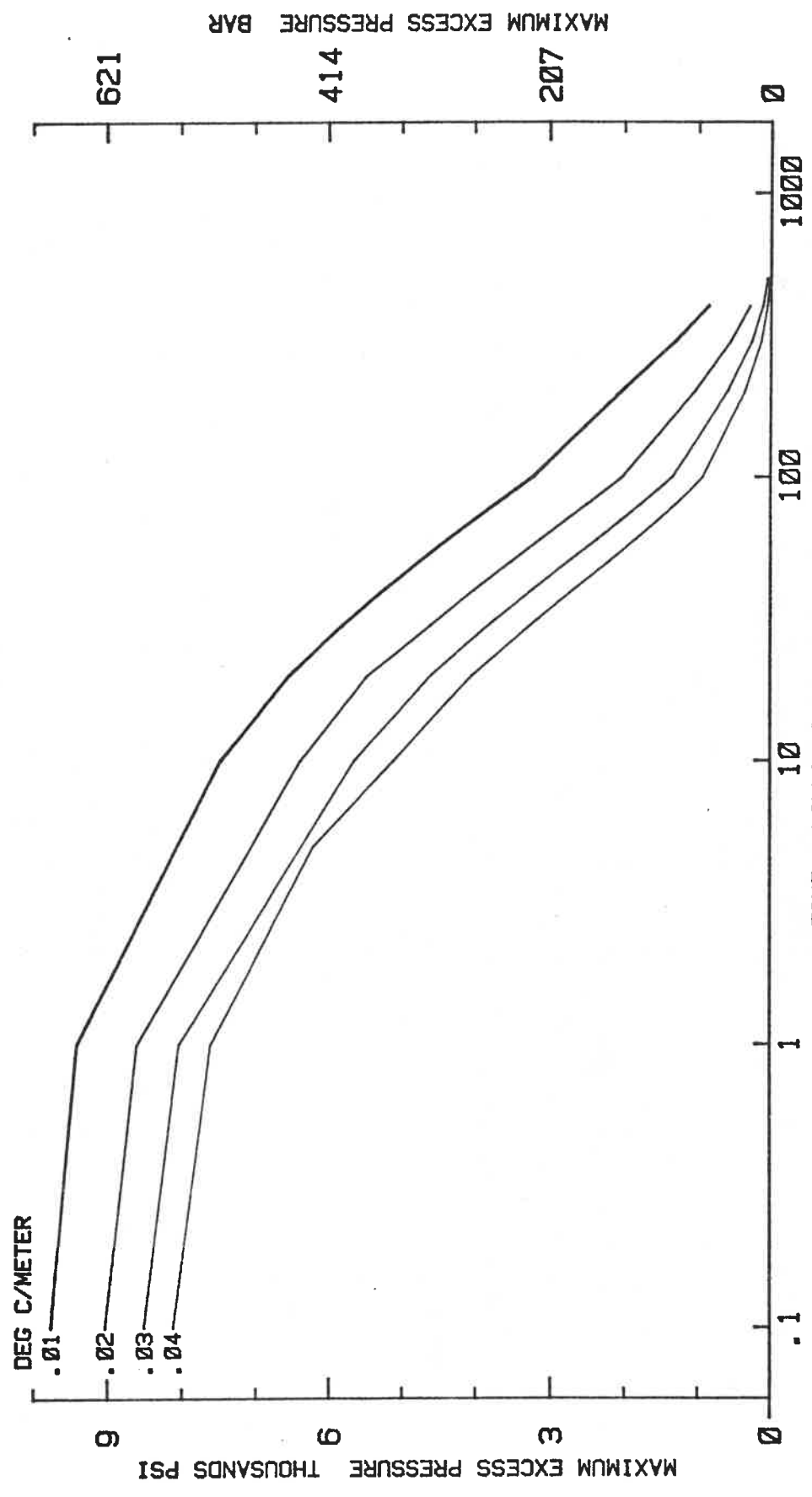
FIGURE 15   INFLUENCE OF GEOTHERMAL GRADIENT ON PERSISTENCE
OF EXCESS PRESSURES IN SHALES
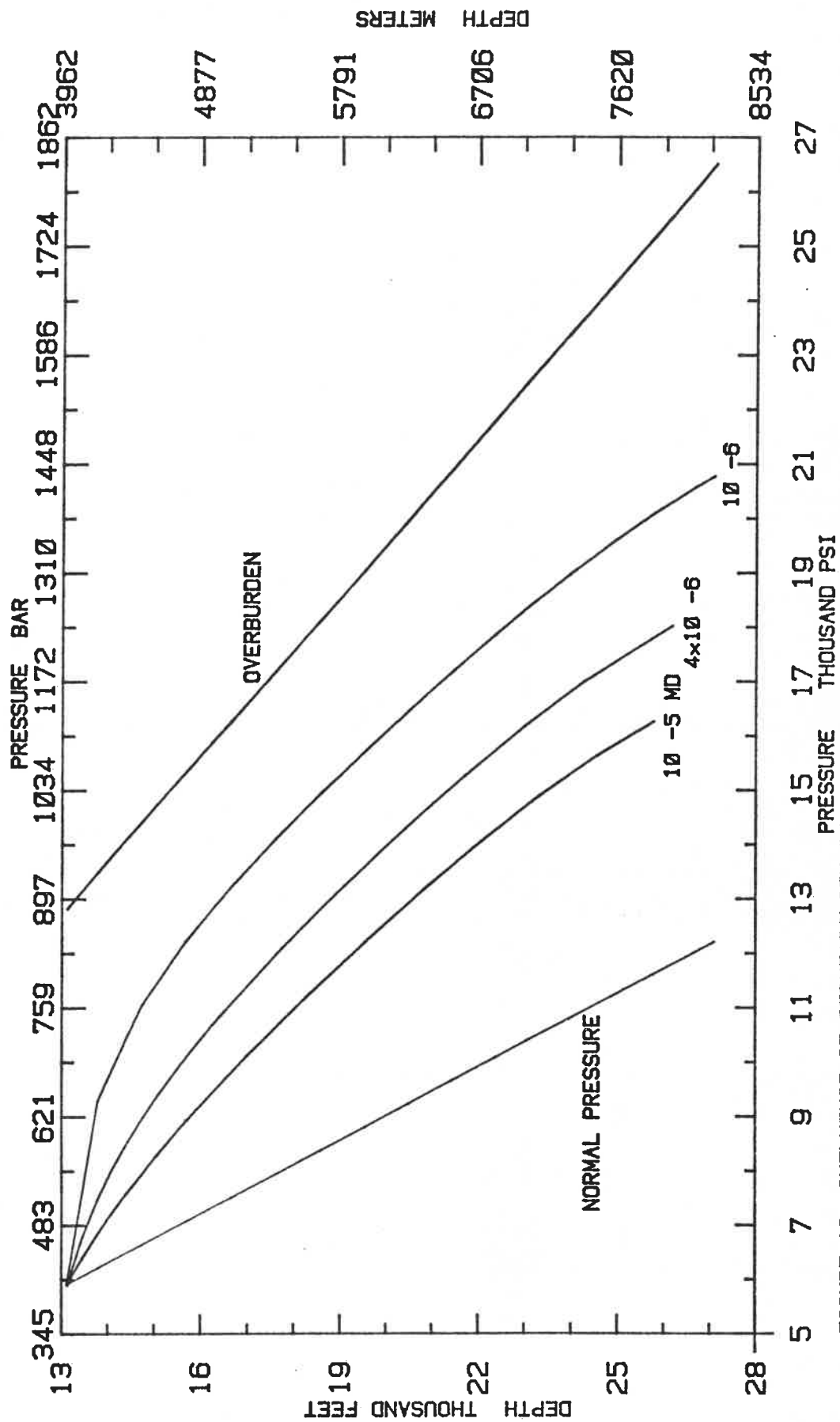
FIGURE 16 INFLUENCE OF PERMEABILITY ON EXCESS PRESSURE IN A SHALE

MAXIMUM EXCESS PRESSURE   BAR

621

414

207

0

1000

100

10

1

.1

TIME   MILLIONS OF YEARS
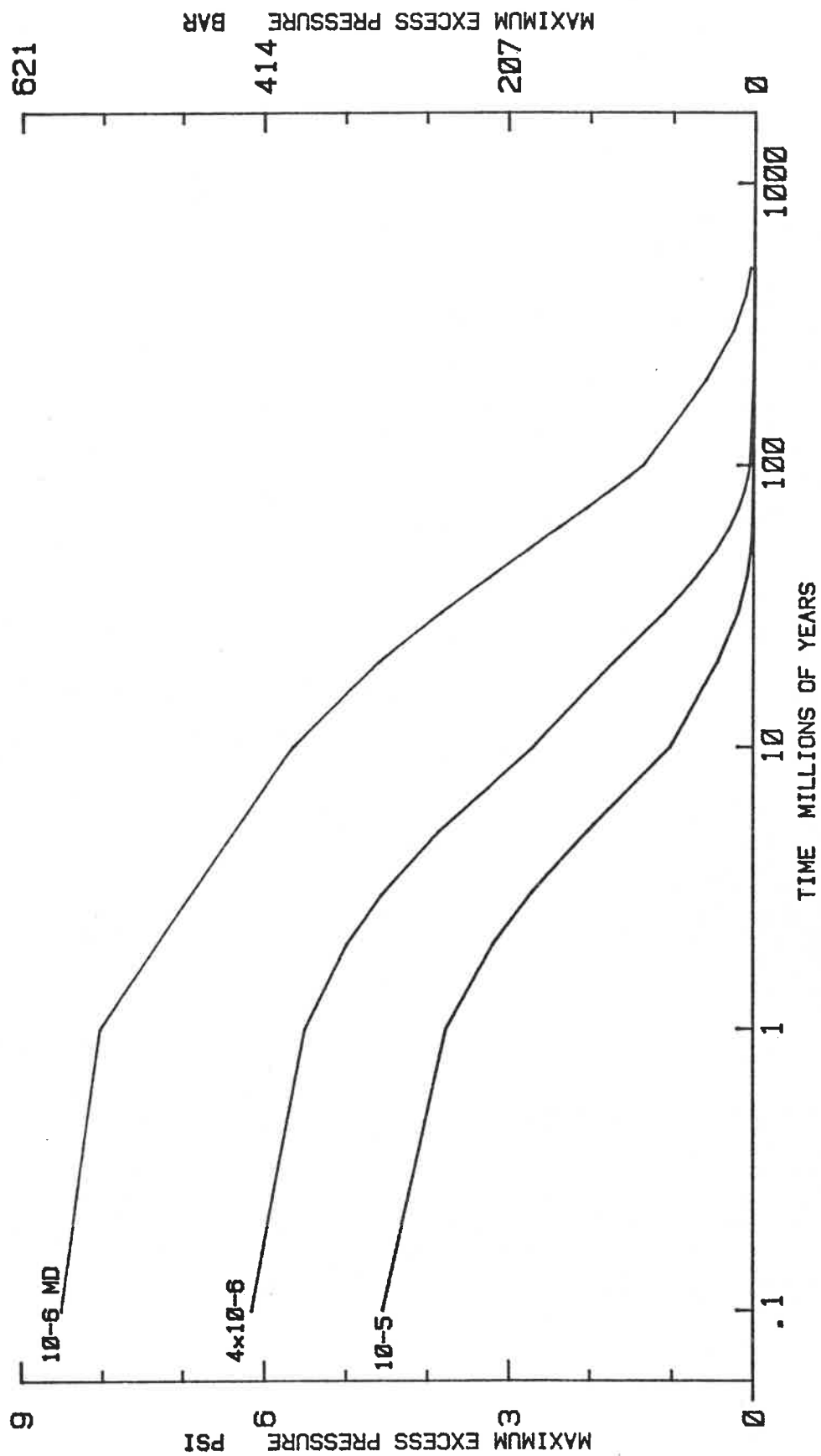
FIGURE 17   INFLUENCE OF PERMEABILITY ON PERSISTENCE
OF EXCESS PRESSURE IN SHALES

10-6 MD

4×10-6

10-5

9

6

3

0

MAXIMUM EXCESS PRESSURE   PSI
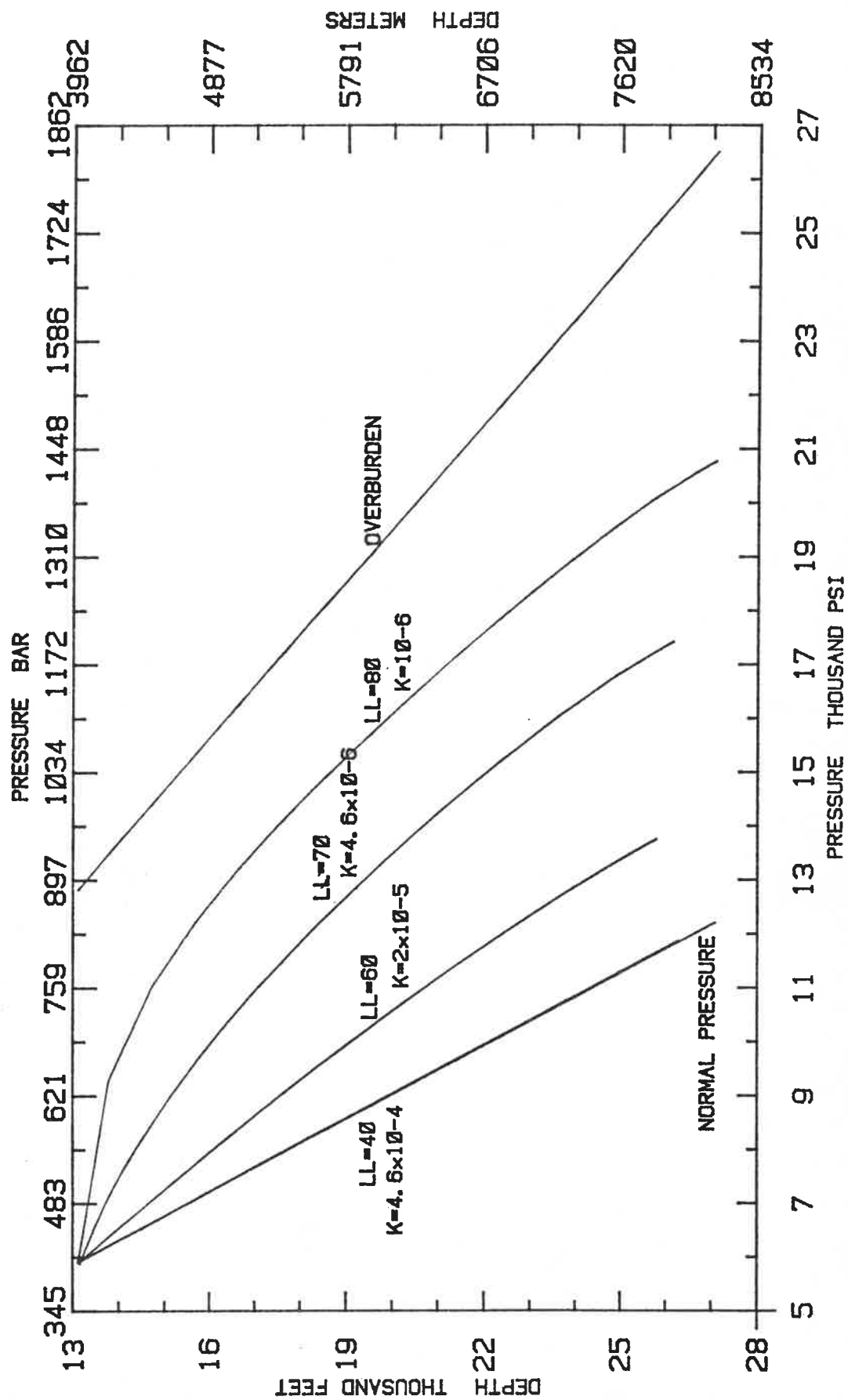
FIGURE 18 DEPENDENCE OF EXCESS PRESSURE IN A SHALE ON THE LIQUID LIMIT AND PERMEABILITY JOINTLY

MAXIMUM EXCESS PRESSURE   BAR

621   414   207   0

TIME   MILLIONS OF YEARS
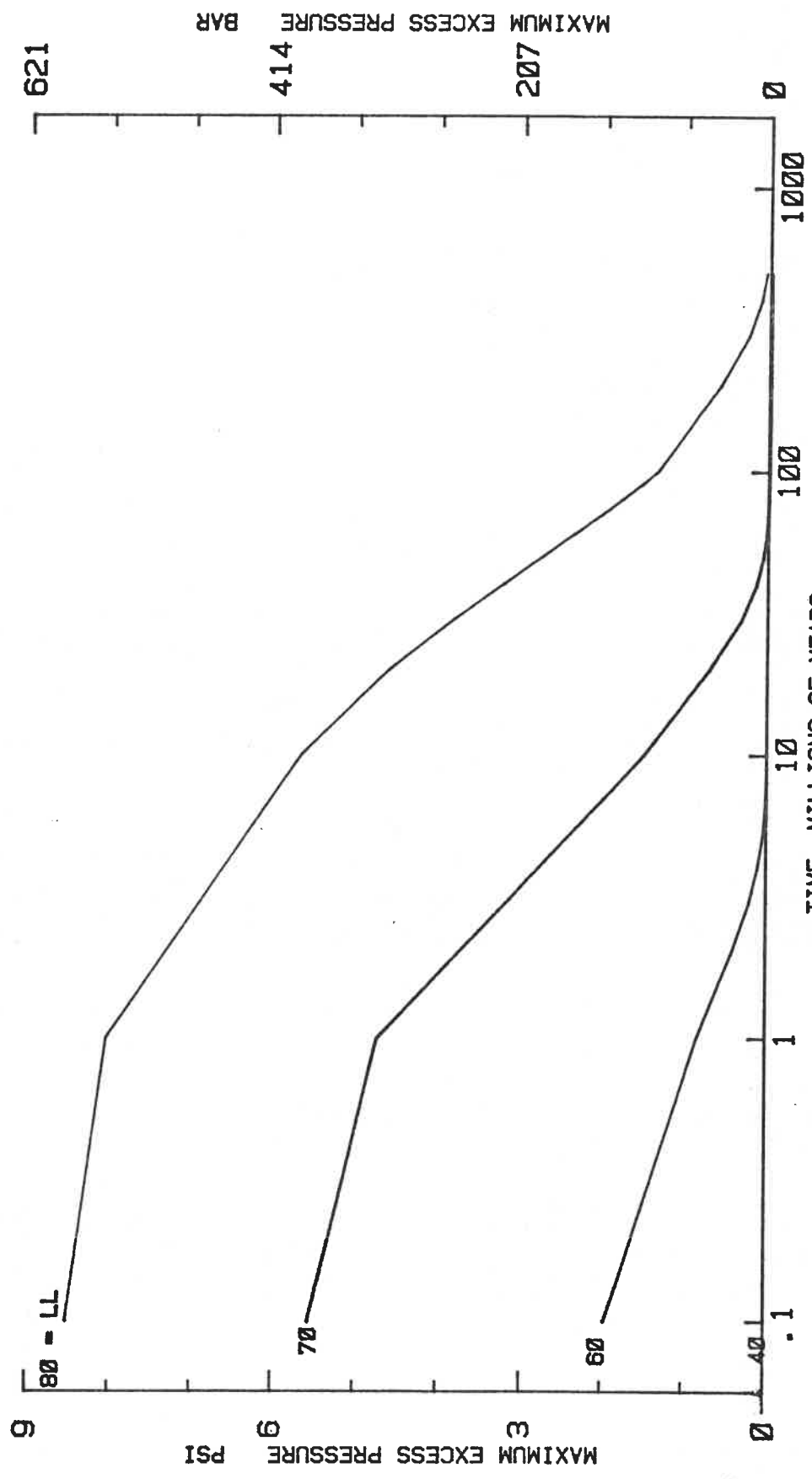
FIGURE 19   DEPENDENCE OF PERSISTENCE OF EXCESS PRESSURE IN A
SHALE ON THE LIQUID LIMIT AND PERMEABILITY JOINTLY

MAXIMUM EXCESS PRESSURE   PSI

LL = 80

70

60

40
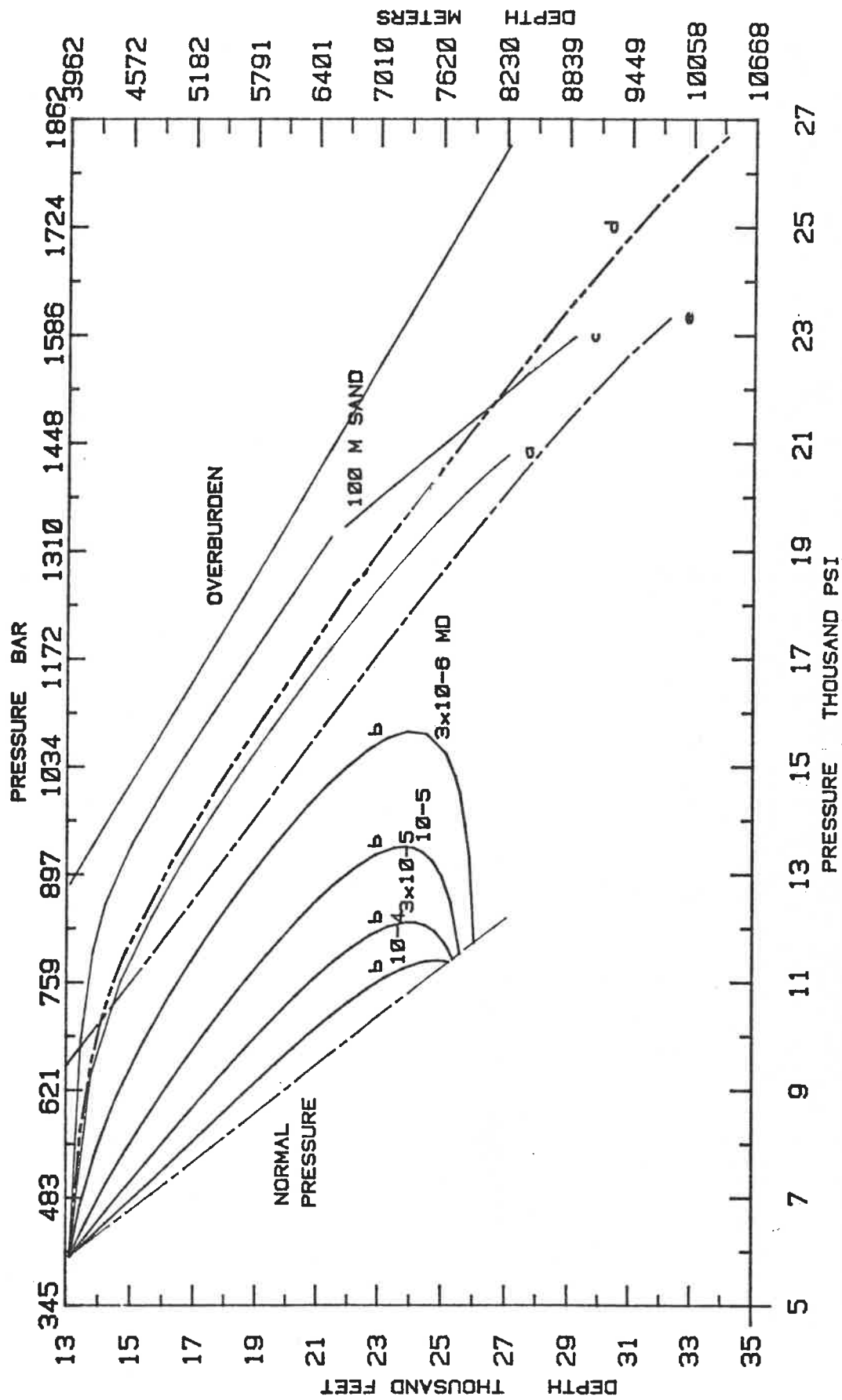
FIGURE 20   DEPENDENCE OF EXCESS PRESSURE IN SHALE ON BOUNDARY CONDITIONS: (a) SHALE UNDERLAIN BY
IMPERMEABLE UNIT (b) SHALE UNDERLAIN BY NORMALLY-PRESSURED SAND (c) SHALE SPLIT BY 100 M
SAND MAINTAINED AT PRESSURE EQUAL TO 95 % OF OVERBURDEN (d) SHALE UNDERLAIN BY ADDITIONAL
1500 M SHALE (e) SHALE BURIED BENEATH ADDITIONAL SHALE.
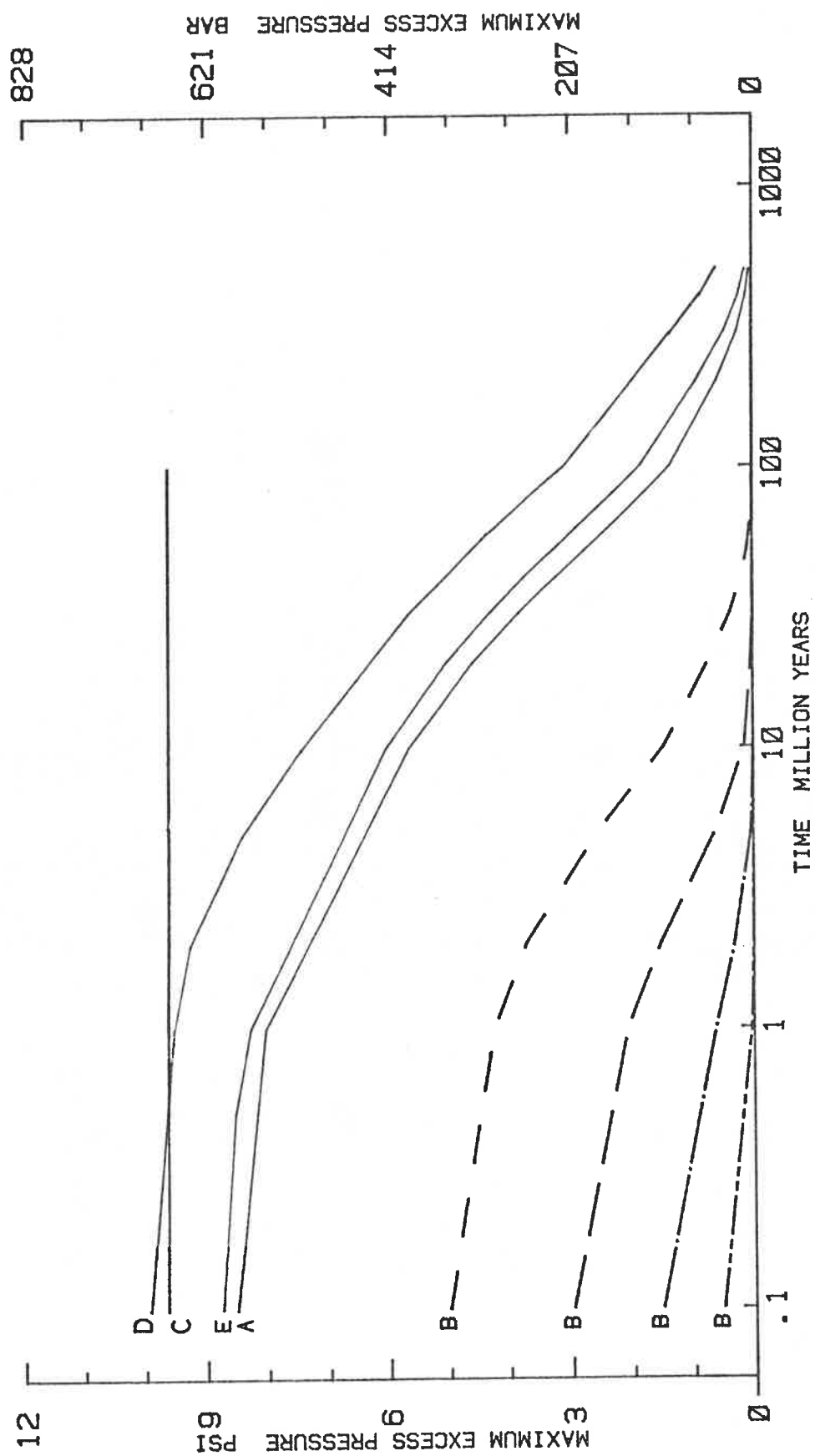
FIGURE 21   DEPENDENCE OF PERSISTENCE OF EXCESS PRESSURES
ON BOUNDARY CONDITIONS
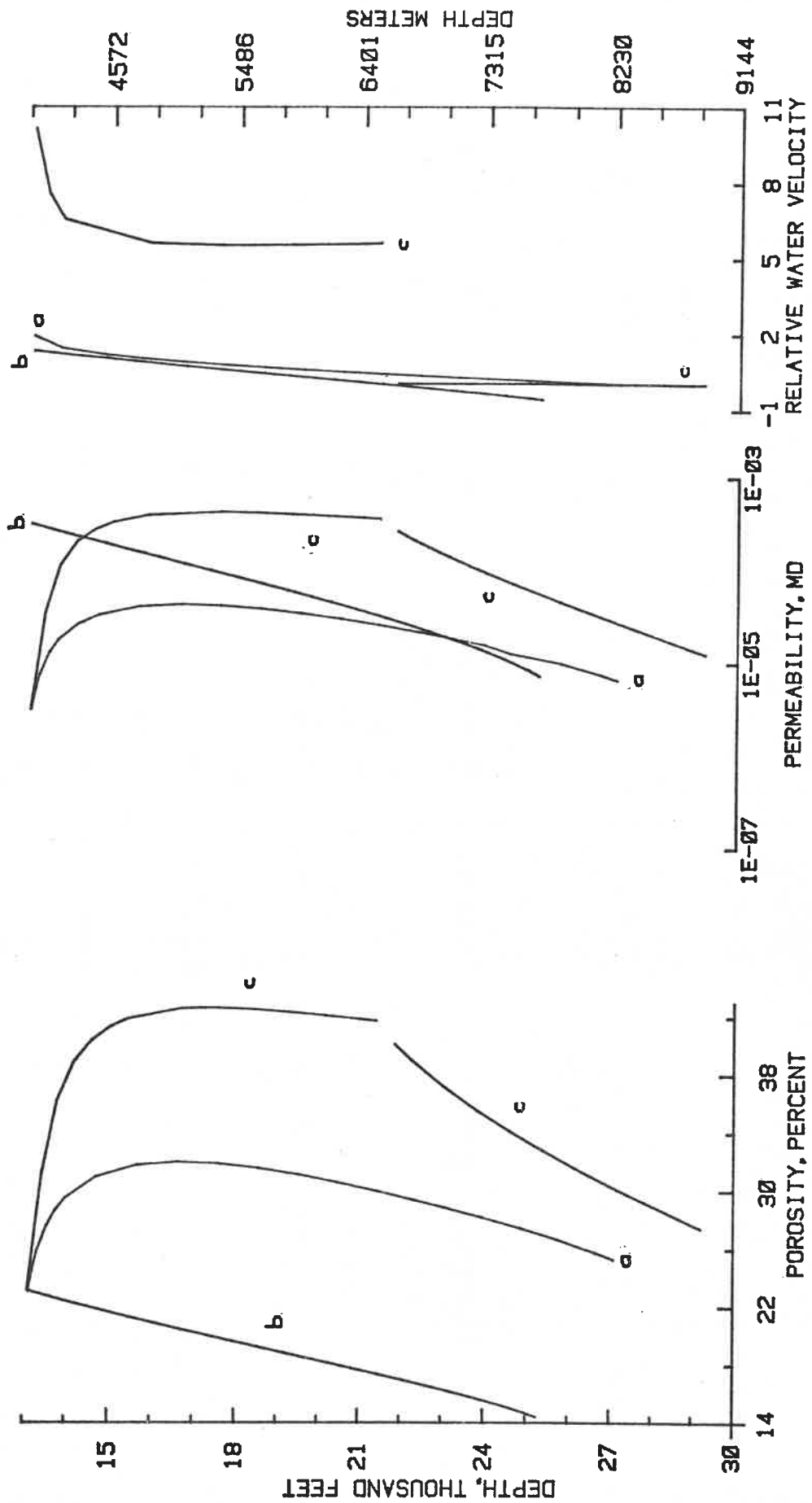
FIGURE 23 INFLUENCE OF BOUNDARY CONDITIONS ON WATER FLOW. LETTERS a, b, and c REFER TO CORRESPONDING CASES IN FIGURES 20 AND 21.
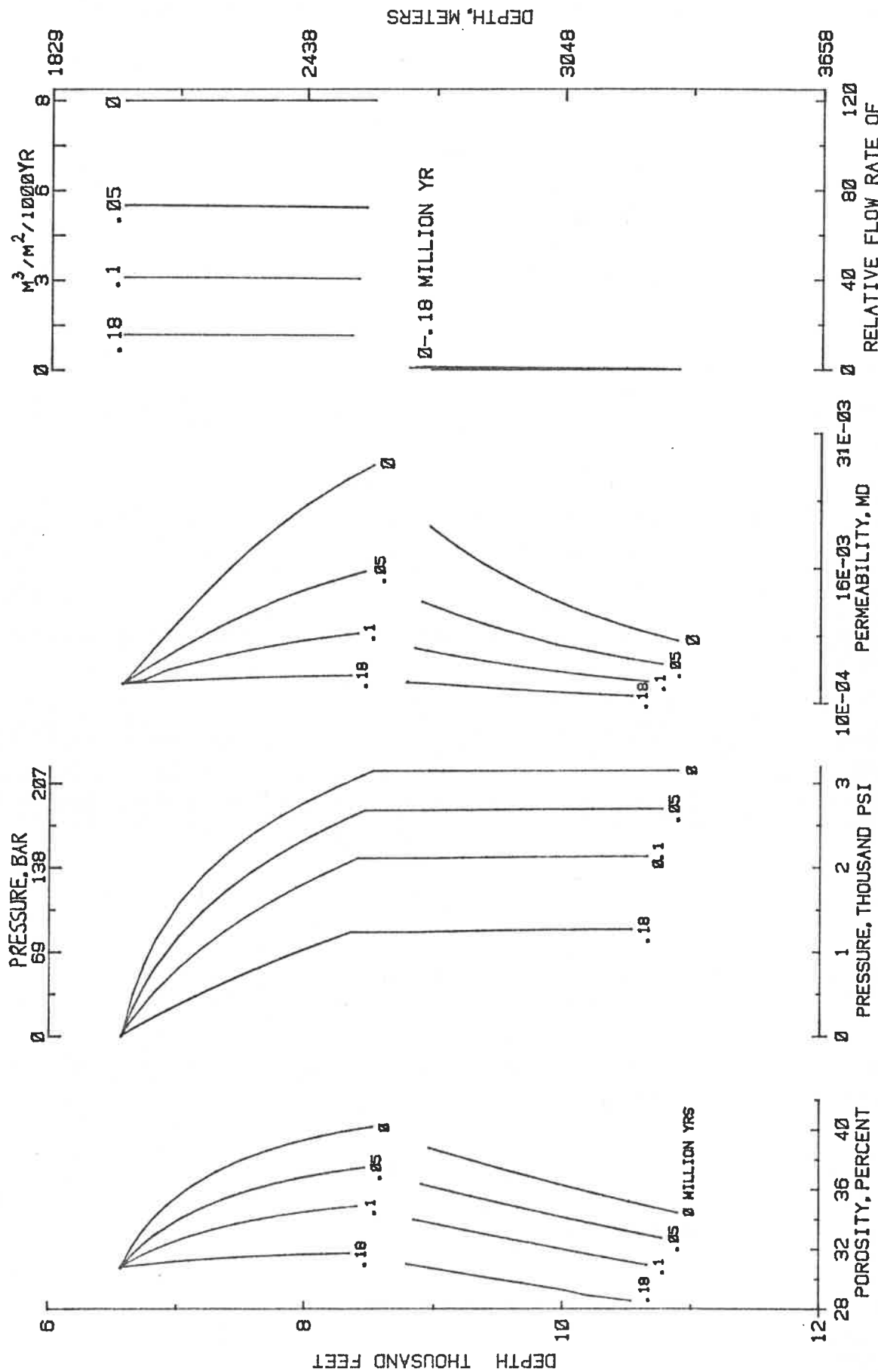
FIGURE 24 DECREASE IN FLOW RATE FROM OVERPRESSURED SAND INTO UPPER SHALE, AND INITIATION OF FLOW UPWARD INTO OVERPRESSURED SAND, UPON GRADUAL REDUCTION OF PRESSURE IN THE SAND.
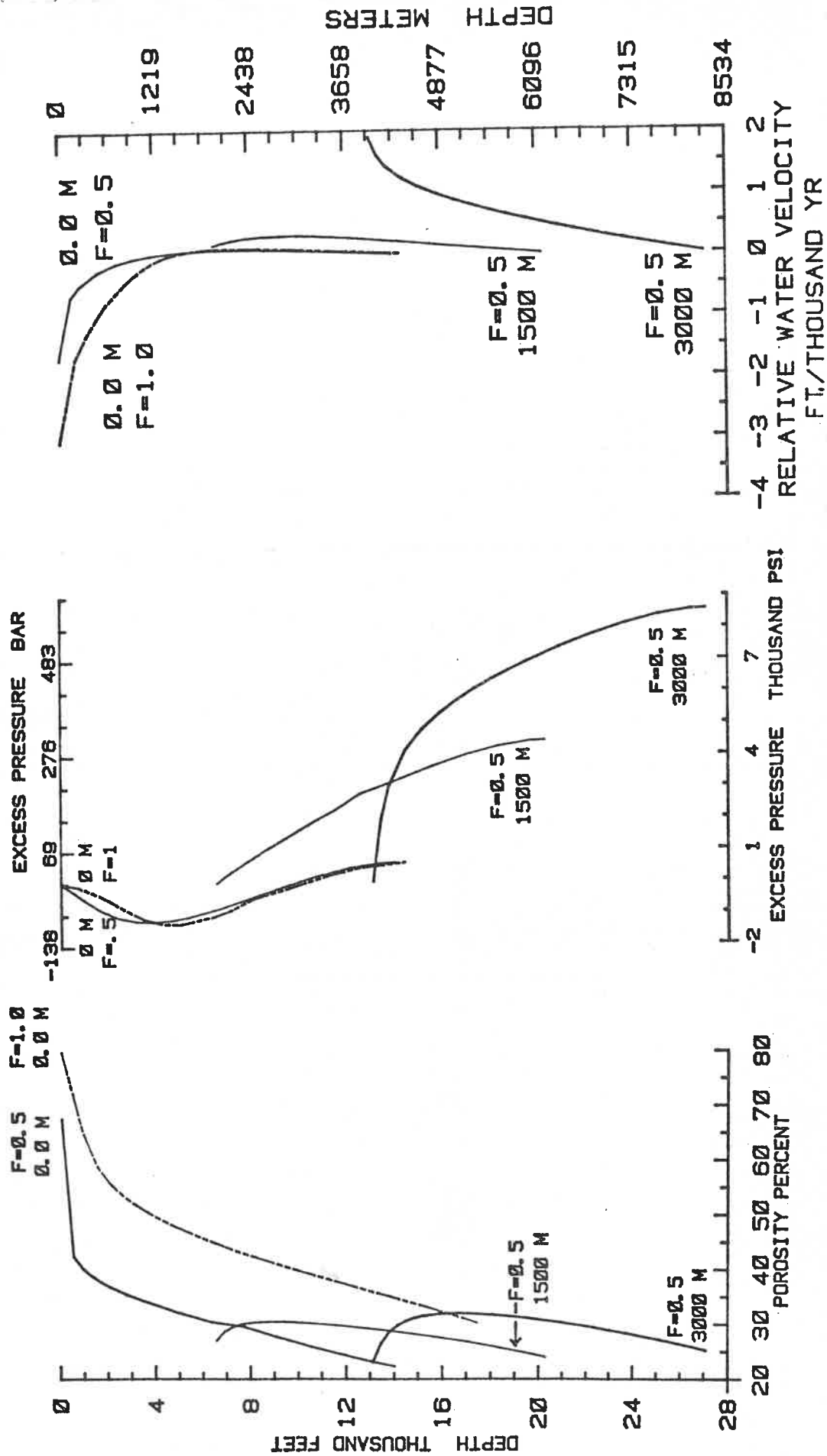
FIGURE 25 CONTRAST BETWEEN THE DEGREE OF DECOMPACTION OF A SHALE WHICH RECOVERS INELASTICALLY AS OVERBURDEN IS REMOVED (SOLID LINE) VERSUS THE SAME SHALE WHICH HAS THE CAPABILITY OF RETURNING ELASTICALLY TO THE ORIGINAL POROSITY DISTRIBUTION (DOTTED LINE).
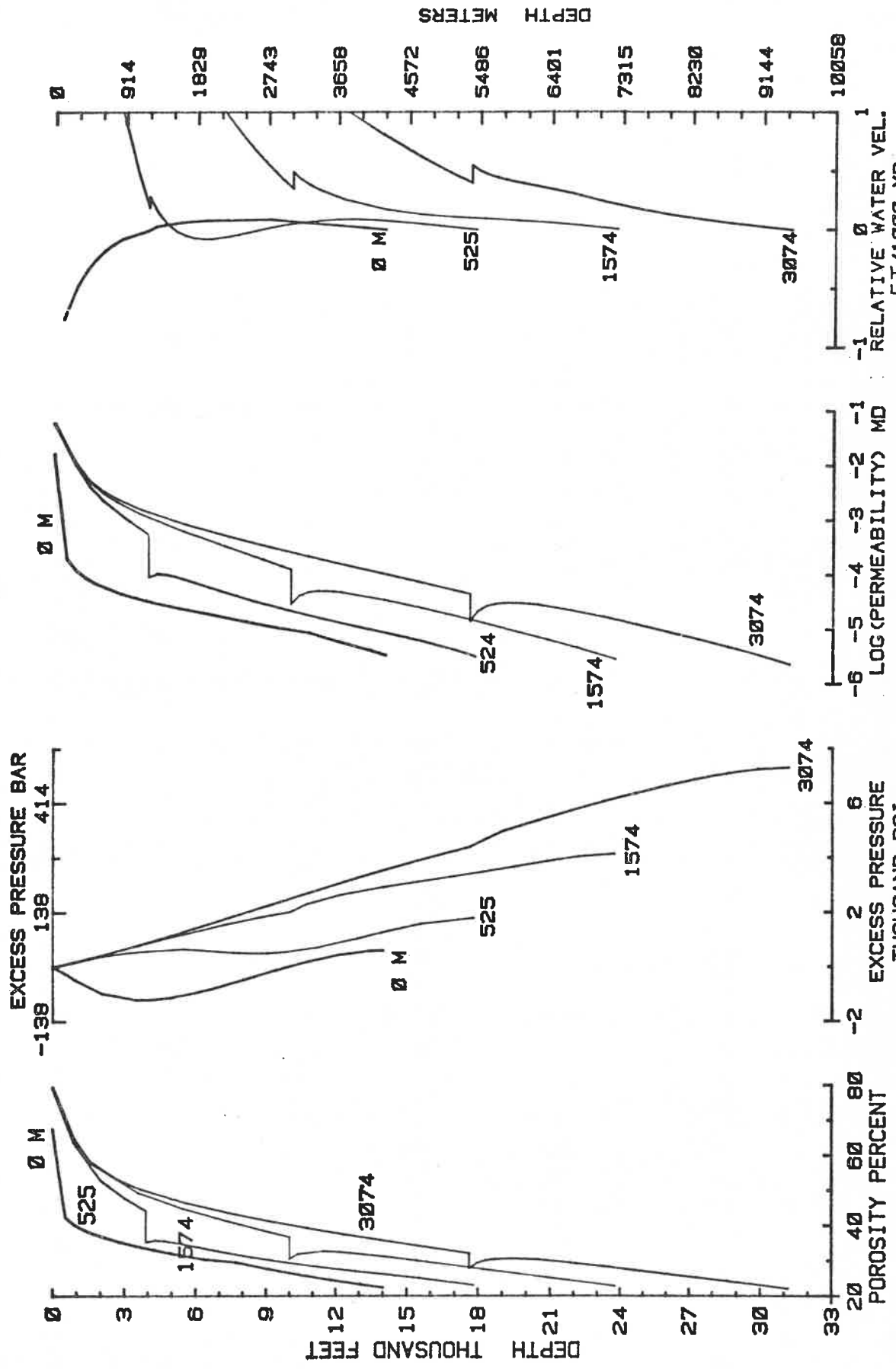
FIGURE 26 DENSITY DISCONTINUITY AT UNCONFORMITY WILL DISAPPEAR AS SKEMPTON-TYPE SHALE UNIT IS RE-BURIED
BENEATH IDENTICAL SHALE TO DEPTH(MATRIX PRESSURES) GREATER THAN ANY PREVIOUSLY EXPERIENCED.
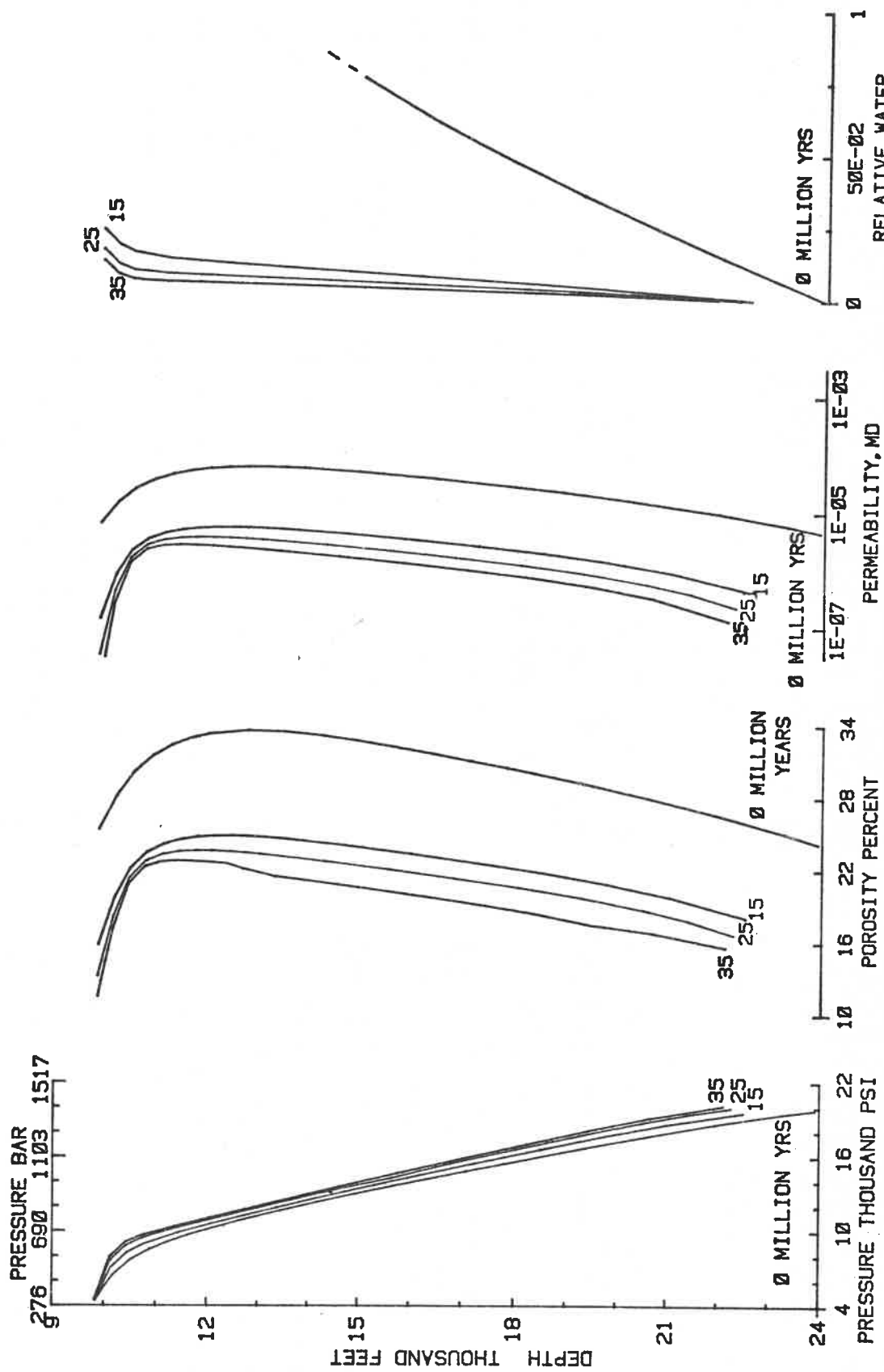
FIGURE 27 PRESSURE DECLINE IN A SHALE FOR WHICH THE GRAIN-TO-GRAIN FORCES DECREASE WITH AGE IS LESS RAPID
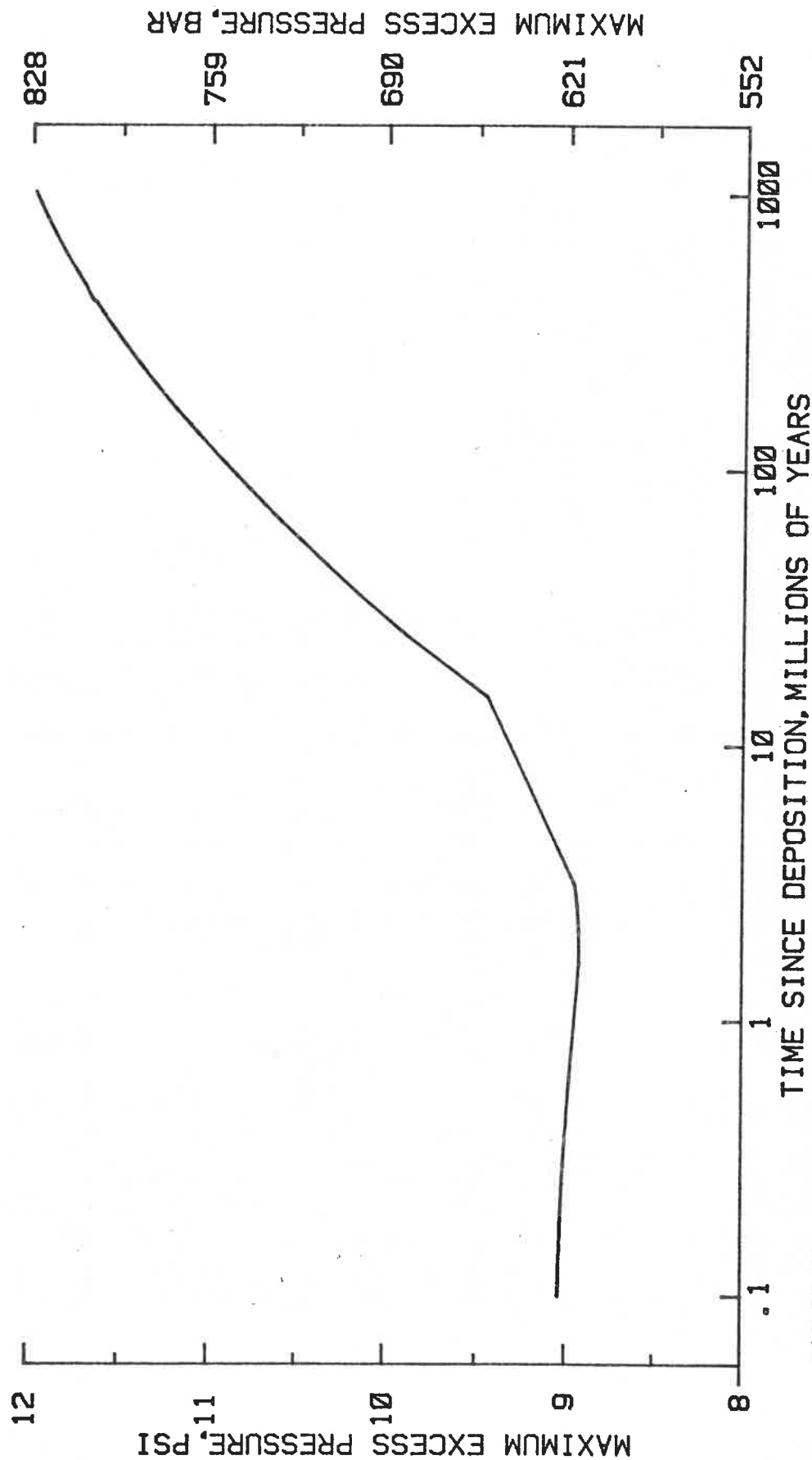THAN FOR A SKEMPTON-TYPE SHALE.

FIGURE 28   THE DECREASE IN EXCESS PRESSURE WITH TIME SLOWS DOWN AND MAY REVERSE BECAUSE, FOR FIXED PORO-
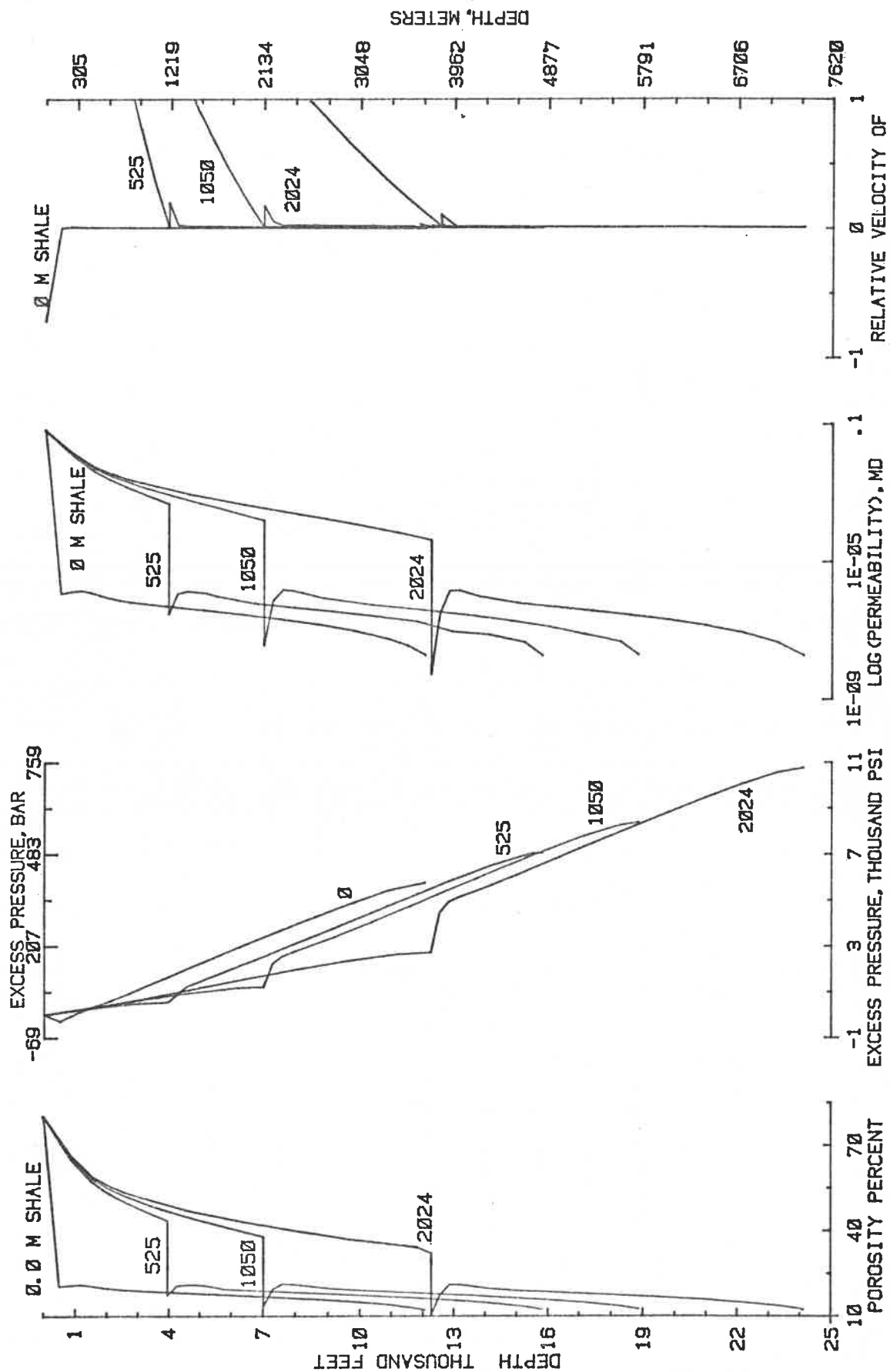SITY, THE GRAIN-TO-GRAIN FORCE, $\varnothing$, DECREASES AS THE SEDIMENT AGE INCREASES.

FIGURE 29   RE-BURIAL OF OLD SHALE UNIT BENEATH NEW SHALE UNIT. PERMANENT DENSITY DISCONTINUITY AT UNCON-
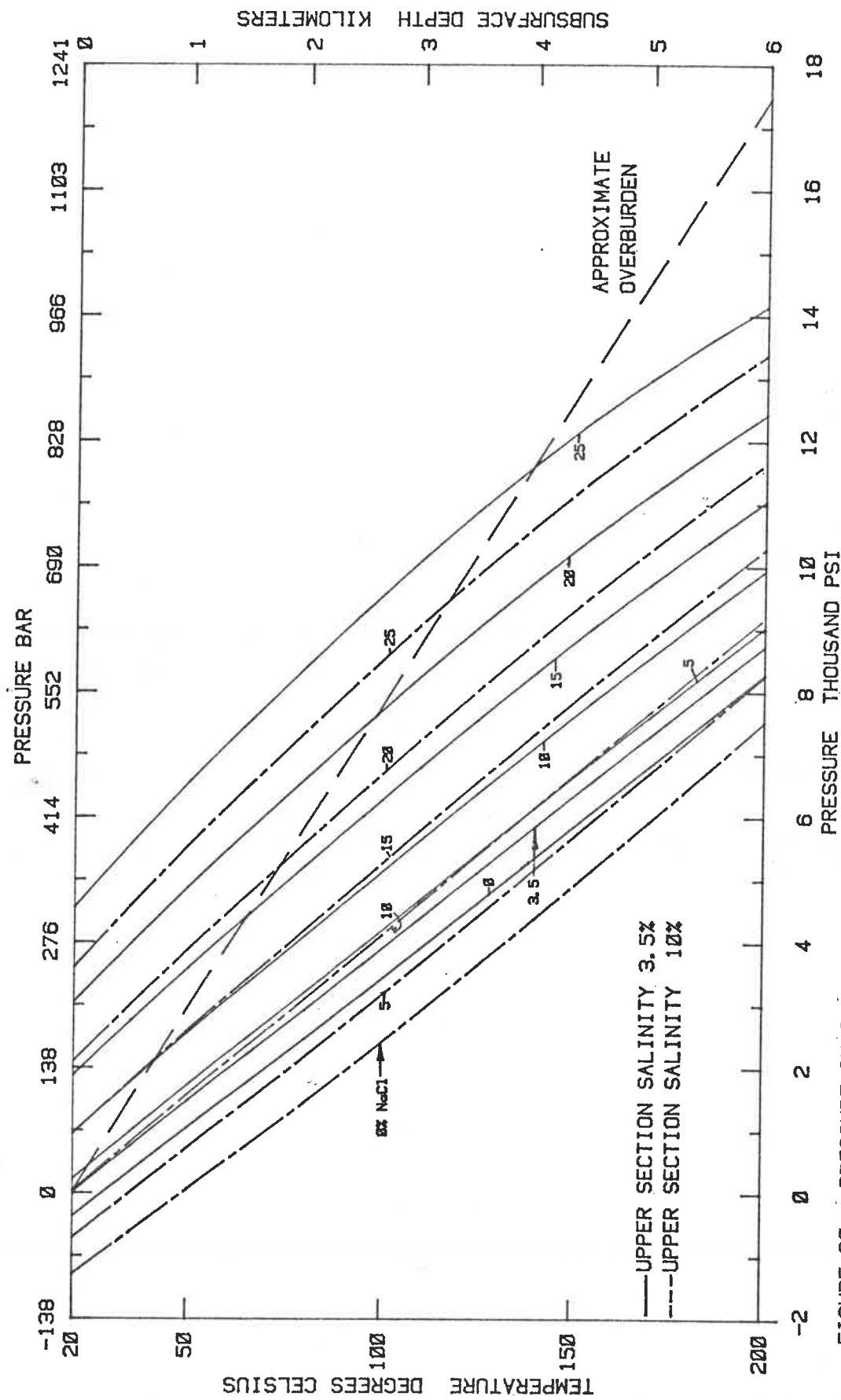FORMITY IS DUE TO AGE DIFFERENCE OF OTHERWISE IDENTICAL SHALES.
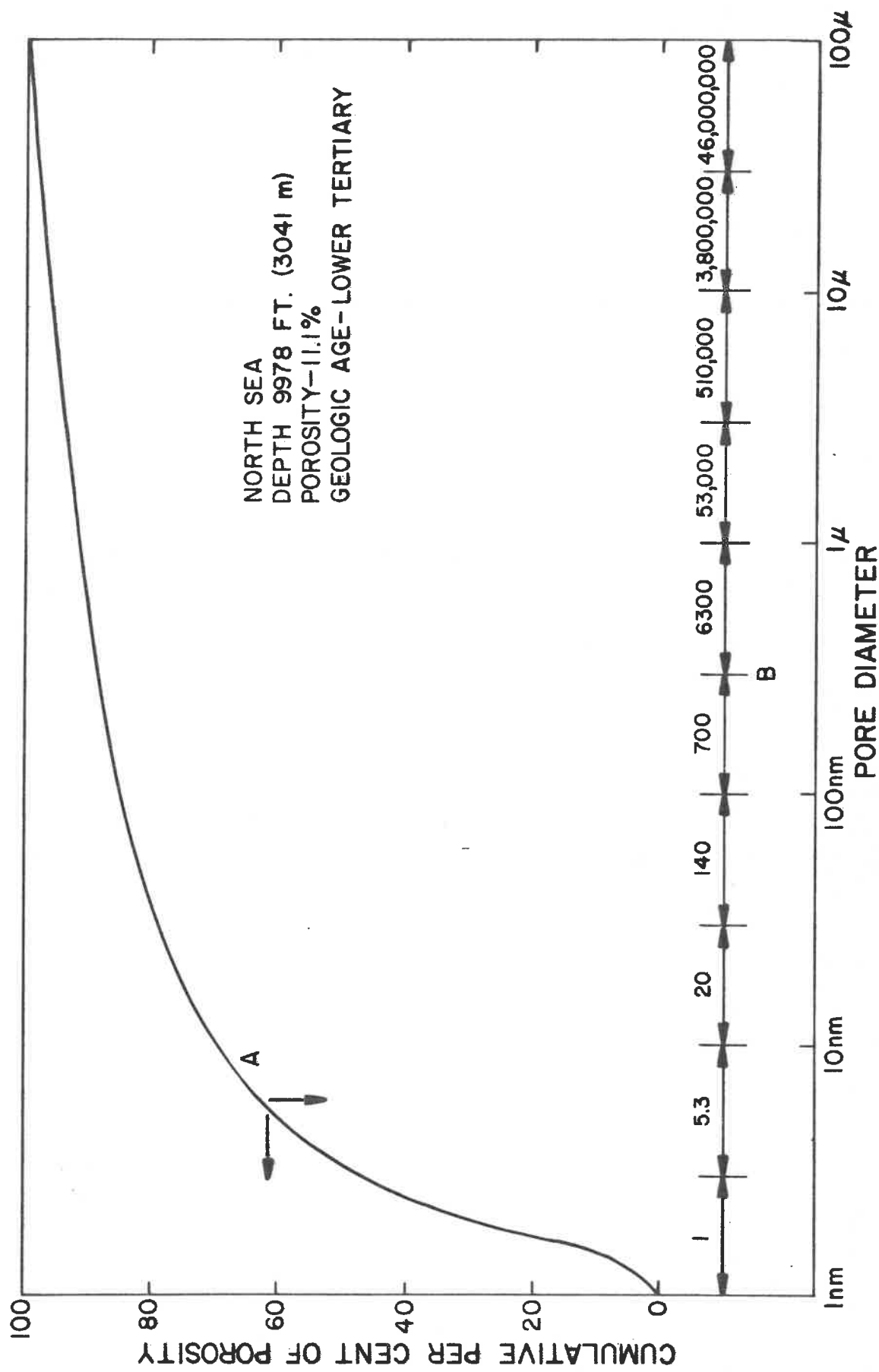
FIGURE 30   PRESSURE IN SAND LENS OF INDICATED SALINITIES, WHEN SEPARATED FROM UPPER SECTION BY 5 M OF SHALE
UPPER SECTIONS ARE NORMALLY PRESSURED AND CONTAIN WATER OF 3.5%(SOLID LINES) OR 10%(BROKEN LINE)
BY WEIGHT OF NaCl.

NORTH SEA
DEPTH 9978 FT. (3041 m)
POROSITY—11.1%
GEOLOGIC AGE—LOWER TERTIARY

PORE DIAMETER

CUMULATIVE PER CENT OF POROSITY

A: CUMULATIVE PER CENT OF PORE SPACE WITH PORE DIAMETERS
   LESS THAN A GIVEN VALUE.

B: RELATIVE VOLUME FLOW RATE THROUGH TUBE BUNDLES WITH
   THE SAME PORE SIZE DISTRIBUTION AS THE SHALE.
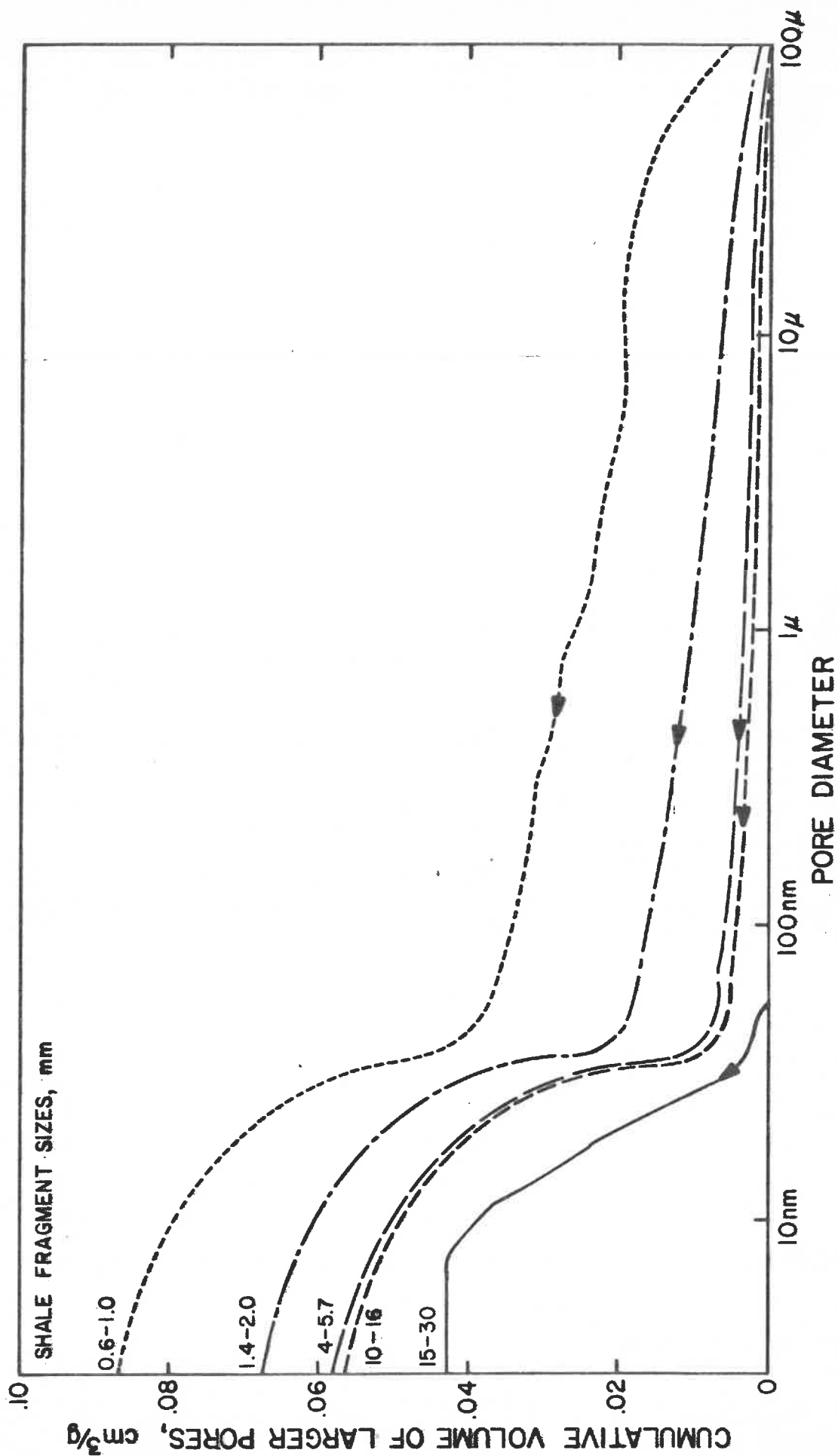
FIGURE 31

FIGURE 32 PORE SIZE DISTRIBUTION OF SEVERAL SIZE FRACTIONS OF SHALE, 10,911 FEET (3326 M), GULF OF PAPUA.